Applied *Nanomaterials and smart Polymers*,
Online ISSN: 2981-0434
Vol. 2, No. 2

ANSP

Review of measurement and analysis of biomarkers using inorganic complexes and metal-based nanomaterials

Saeideh Hosseini [1]*

[1] Independent researcher, Ph.D. of Inorganic chemistry, Zanjan, Iran, ORCID ID.0000-0001-9865-4624

ABSTRACT

Biomarkers are biochemical/physiological changes in body tissues or fluids that can be accurately and reproducibly measured. They can indicate the entire spectrum of the disease and potentially the choice of the type and dosage of drugs can increase the effectiveness and minimize effective therapeutic interventions. Therefore, the identification of biomarkers is of particular importance in the development of pharmaceuticals and moving towards personalized medicine.

Nanotechnology as a new scientific field with novel combinations has taken the lead in the fields of medical diagnosis, imaging and therapeutic applications. Investigation of literatures determined that signal generation probes based on inorganic complexes and metal-based nanomaterials can generally be one of the suitable candidates for diagnosis. Therefore, in this study, the importance of using inorganic chemistry and nanotechnology in the field of identifying biomarkers has been discussed. In the first part of the review, the main definitions in this field have been explained. Then, a set of biomarkers associated with a specific disease and number of methods for measuring biomarkers are described. In the next section, the use of inorganic metal complexes and nanoparticles in probes for sensing and imaging is discussed and finally, current challenges and future prospects are presented.

Keywords

Biomarker, inorganic metal complexes, inorganic nanoparticles, imaging modalities, metal-based signal generation probes, nanotechnology.

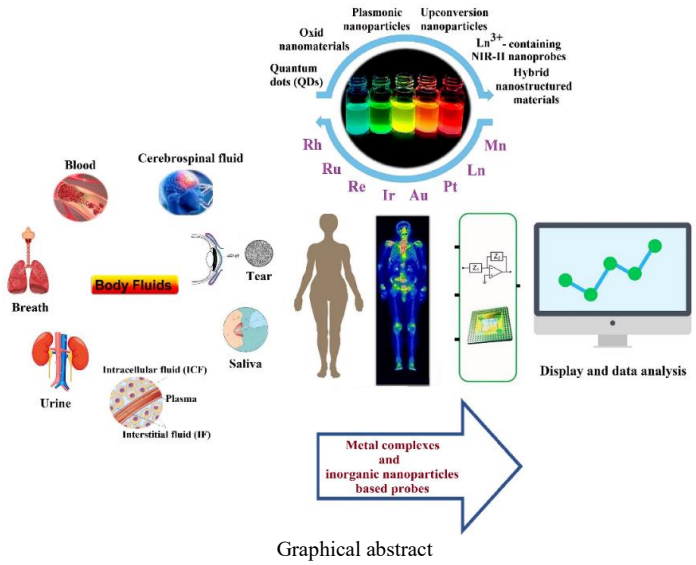

Graphical abstract

* Corresponding Author Email: hsaeideh@gmail.com

1. Introduction

The definition of biomarker dates back to the 1950s [1,2] In 1987, " Markers of signaling events in biological systems or samples" were introduced as biological markers [3]. In 1990, biomarkers were defined by McCarthy and Shugart "Measurements at the molecular, biochemical, or cellular level in wild populations from contaminated habitats or in organisms experimentally exposed to pollutants that indicate that the organism has been exposed to a toxic chemical and indicate the extent of the reaction of the organism." [4]. In 1994, a biomarker was pointed by Deplage as "a biochemical, cellular, physiological, or behavioral change that can be measured in tissues or body fluids or at the level of the whole organism that indicates exposure and/or effects of one or More contaminants." [5]. In 1996, biomarkers were stated by Gestel and Brummelen. According to this definition, a biomarker should by definition be used only to describe lethal biochemical changes caused by exposure to xenobiotics [6].

Given the increasing global importance of biomarkers in modern healthcare, in 1998 the Biomarker Definitions Working Group of the US National Institutes of Health (NIH) defined a biomarker as: "a feature (molecular, histological, radiographic, or physiological) that is measured and appraised as an representative of normal biological and pathogenic processes or pharmacological repercussion to a therapeutic intermediation" [7-11].

In 2000, the phrase biomarker appointed by De Lafontaine as: "primary responses to biochemical and/or physiological change(s) in organisms exposed to pollutants [12]. Therefore, accurate and reliable detection of biomarkers is very important for early diagnosis of the disease and thus the possibility of timely treatment [13,14].

William Osler (one of the founders of modern American medicine) has a theory in which pointed out the importance of diagnosis: "Diagnosis over medication is our priority." [15]. Biomarkers have a substantial role in the diagnosis and management of cardiovascular diseases, infections, immune and genetic disorders, and cancer [16].

1.2. Types of biomarkers

Many biomarkers have been reported in the literature and used in diagnostic products. They can be found in body fluids such as blood, serum, urine, saliva, tears or cerebral spinal fluid [17]. Biomarkers include changes in anatomy (bone density or tissue fluid balance), pharmacological actions, formation of metabolites (e.g. metabolomics, proteomics, glycomics, lipidomics), changes in enzyme rates, urinary and blood-related additional compounds, Blood glucose, amino acids, Nucleic acids [18]. disease-specific molecules such as pathogen-specific proteins, host response molecules (immunoglobulins) [17]. arachidonic acid cascade and especially factors derived from leukotriene B4) [18-20]. An increase in the amount of metal ions (copper, zinc, iron and aluminum) in the brain [21] and other cases [13,14].

1.3. Measurement of biomarkers

Measurement of biomarkers can help to explain the experimental results of clinical trials as well as the development and evaluation of new treatments. There are different methods to measure biomarkers [22] a range of techniques such as flow cytometry, polymerase chain reaction (PCR) Western blotting, (ELISA) enzyme-linked immunosorbent assay, atomic force microscopy (AFM) Fourier transform infrared spectroscopy (FT-IR), electron microscopy, gel electrophoresis, Nuclear magnetic resonance (NMR), Chromatography and mass spectrometry (MS) [13, 21,23,24] light scattering methods and X-ray absorption spectroscopy. [21] Molecular imaging is another measurement method that will be discussed further [25]

1.4. Biomarkers & imaging modalities

Molecular imaging is an incredibly diverse field and defined as the representation, identification, and quantification of biological processes and physiological status at the molecular and cellular levels in humans and other living systems and produces highly predictable clinical value. The emergence of molecular imaging as a scientific discipline is the result of advances in chemistry, biology, physics, and engineering and the application of imaging probes and technologies. The impact of molecular imaging on pharmaceutical sciences and clinical medicine has been extensive, because it helps in better diagnosis and as a result providing more effective treatment as well as monitoring its effectiveness, and on the other hand, it allows pharmaceutical companies to reduce the time required to introduce new therapeutic drugs to the market [18,25] Some of the methods are used for clinical applications include X-ray imaging,

mammography, CT scan (computed tomography, axial computed tomography or CAT), PET (positron emission tomography), single photon emission computed tomography (SPECT), PET/CT and SPECT/CT scanner, magnetic resonance imaging (MRI), MR, MRS, ultrasound imaging, fluorescence-based imaging, photoacoustic imaging, each of which has its strengths and limitations [17,18], [20,21,23]. [26-30]

1.5. Leveraging Inorganic Chemistry for Detection

Inorganic metal complexes and nanoparticles have been widely used in biomedicine due to their particular optical, electrochemical, magnetic and catalytic properties. signaling methods (signal-producing probes) in diagnostics and have been used in contrast MRI, in vivo bioimaging, photoluminescence, electrochemical sensing platforms, and electrochemiluminescence (ECL) are among the biomedical applications. [15].

Inorganic complexes have unique chemical and photophysical properties that mainly depend on the identity of the metal center and the chemical structure of the ligands [31] long-lived phosphorescence [15, 32]. significant (large) Stokes shifts [14,33], high photostability, wide emission range, emission tuneability (tunable emissions) [15,34] Ability to withstand greater changes in pH and temperature, [35]. The possibility of regulating their chemical nature based on biological properties (membrane permeability, localization of organelles and/or interaction with specific biomolecules), [13] Ability to be conjugated with biological carriers in order to create cellular specificity and increase sensitivity [31] are among the advantages of inorganic Photoluminescent complexes that have caused photoluminescent mineral complexes to appear as attractive candidates for biological probes as signaling molecules for detection, [15,36]. Designing and leveraging coordination chemistry to prepare bright metal-based compounds is an exciting research proposal that is currently being explored by many [31,34,37] General reviews on the use of metal complexes for sensing have been published by various groups [38]. [31,39].
In this review, a summary of all the data collected from the literatures in Table 1 and provide insights into the future potential of these compounds for the investigation and treatment of human diseases.

Table 1. Typical Examples of detection platforms based on luminescent Inorganic metal complexes.

Luminescent probe	Application	References
Manganese (II) terpyridine complex	Suitable for use in two-photon fluorescence microscopy and MRI.	[40]
Rhenium(I) polypyridine isothiocyanate and maleimide complexes	Used in the development of various bioassays.	[31,41,42]
Rhenium(I)-dipyridophenazine complex	“Switch-on" probe for double-stranded duplex DNA.	[43,44]
Rhenium(I) complex conjugated with folic acid and PEG	Tumor cell marker	[42]
$[Ru(bpy)_3]^{2+}$ and $[Ru^{II}(bpy)_2L]^{n+}$ complexes	Detect anions, metal cations, highly sensitive applications in immunoassays and DNA assays	[42,45,46]
Ruthenium (II) complexes with 1,10-phenanthroline and bathophenanthroline derivatives	Environmental and biological HClO probing	[37,47]
Guanidinium group modified bipyridine-Ru(II) complex	Luminescent probe for the c-myc G-quadruplex	[35,45]
Ru(II) complexes conjugated with crown ether moieties	ECL sensors for metal ions.	[42,45,48]
cyclometalated Iridium (III) complexes	Suitable probes for LD visualisation in live cells and organisms, discrimination of Cys from other biothiols such as Hcy and glutathione (GSH)	[31,49]
Iridium(III) complexes with thiaaza and aza crown ether-substituted phenanthroline-based ligands	Multi-cation detection in single or multi-channel detection protocols.	[48]
Iridium (III) complexes functionalized with specific recognition elements	Detection of metal ions, small molecules, proteins, enzymes and cancer cells.	[50,51]

Table 1. continued

Luminescent probe	Application	References
Pt(II) based probes containing 4-amino-1,8-naphthalimide moiety	Bacteria imaging	[52]
Pt(II) complexes in the general form $[Pt^{II}(C^N)L]^{n+}$, $[Pt^{II}(C^N^N)L]^{n+}$	luminescent light switch for c-myc G-quadruplex DNA selectivity towards HSA	[52]
Pt(II) complexes with a central aromatic scaffold with pendant amine side chains	Luminescent probes for G-quadruplex DNA	[53]

Au(I)-phosphine complex containing a naphthalimide ligand	Promising candidates for imaging	[53]
Tetrakis(diisopropylguanidinio)zinc (II) phthalocyanine	Fluorescent probe for c-myc G-quadruplex	[54]
Lanthanide complexes using chromophores containing pyridine, carboxylate, ß-diketone group, salophene, etc.	Cell imaging	[31,55-59]

The vast majority of metal-based probes and nanoparticles produce optical signals such as absorption, fluorescence or phosphorescence. Consequently, a multiple assemble of precision tools has been developed for quantitative imaging and quantification purposes [15,60] These nanoparticles offer several important advantages including high quantum efficiency, size-dependent emission tunability, and enhanced photostability Conjugation with biomolecular targeting ligands (antibodies, aptamers, peptides or small molecules), high sensibility, good specificity, Cost-effective and easy assimilation, [17,60-62] cause Nanomaterial-based electrochemical biosensors as the most attractive type of biosensors which used in medical, environmental, food and other fields, [63-65], To date, several nanomaterials, Quantum Dots (Colloidal semiconductors), [15,17,18,29], [62,63] [66-70] metal oxide nanoparticles (CuO, ZnO, magnetice), [17,60,63,71] Up conversion nanoparticles (UCNPs), [17,72,73] plasmonic nanoparticles, including noble metal nanoparticles (Gold and Silver nanoparticles). [15,17]. [61,63,68,74] NIR-II nanoprobes containing Ln^{3+} [75] have been used for production and Amplified signals electrochemical biosensors.

1. 6. Hybrid Metallic Composite Nanostructures as Recognition Elements

Hybrid nanostructures offer distinct advantages compared to individual components and at the same time, it is possible to find new properties and functions for practical applications. Hybrid nanostructures have been used as immune probes to detect biomarkers. The components of a hybrid nanostructure can be chosen from a wide range of materials. [23] for instance, nanoparticles doped with lanthanide chelates, [15] nanoparticles consisting of latex particles, silica-based beads or inorganic lanthanide doped phosphors, [76] Metal nanoshells such as: (CdSe/CdS/ZnS), ZnS-CdS@MoS_2 /chitosan nanocomposite, Au@Ag core-shell colloids, Fe_3O_4/Au/Ag nanocomposites, Ag@SiO_2@SiO_2-RuBpy, (Fe_3O_4@nSiO_2@mSiO_2 @Aptamer) nanoparticles, Au/TiO_2 nanocomposite, TiO_2 nanosilk@MoS_2, [23,61,63, 68,77,78], The integration of inorganic complexes with nanomaterials such as metal- organic framework (MOF) is one of the approaches that can be used to develop the next generation of detection probes, [15,79-81]

2. Materials and methods - Search Strategy

In this study, the keywords i.e., Biomarker, inorganic nanoparticles, inorganic nanoparticles, metal-based signal generation probes were searched in various databases such as Scopus, Google Scholar, PubMed and ISI. The related articles written regardless of the time limit and based on the use of complexes and inorganic nanoparticles in diagnosis were evaluated and used to write this research.

3. Conclusions

As discussed, biomarkers are of great importance in biomedical research, including the drug development process and therapeutic evaluation strategies by understanding the relationship between measurable biological processes and clinical outcomes. The more understand about the nature of a disease process and the drug pharmacology that affects it, we will be able to make progress in diagnosing, staging, and monitoring disease and its response to treatment. At least since the 1980s, the need to use biomarkers in diseases such as cancer, cardiovascular diseases, infectious diseases, as well as diseases related to neurology and psychiatry has been widely discussed. The use of biomarkers in basic and clinical research, as well as research on potential new biomarkers for use as surrogates in future FDA trials, is a growing trend. In order to provide health care and quality of life in an optimal way, it is necessary to design innovative, Cost-effective, easy-to-use, and effective solutions. In this way, it becomes possible to check the health status and factors affecting the health by the patients themselves and their companions. Recent advances in medicine help in understanding various types of diseases, thereby making more accurately diagnose and choose treatment, as well as monitor the procedure of the disease.

In this review, the use of luminescent transition metal complexes as labels and probes for biomolecules has

been highlighted. Examples have shown that the use ofmetal complexes in luminescence probes due to their rich photophysical properties is a promising field in the detection and identification of biomarkers and has a very bright future. In summary, with the targeted selection of metal centres and ligands, biologically-relevant substrates and reactive functional groups, transition metal complexes can contribute to a wide range of biological applications. Due to the amazing and fascinating properties of inorganic nanoparticles, they are usually used as powerful sensors and probes for the sensitive and selective detection and quantification of important biological analytes, and it is an attractive and fast-growing research field. Over the past few years, significant achievements have been made in the construction of biosensors. However, there are still opportunities for further development and acquisition of unique properties in nanomaterials in various fields, which are worth in-depth and systematic research. In this context, the use of new nanoparticle manufacturing techniques can lead to new optical properties that can be used for the development of theranostic nanomaterials. In the future, various developments can be envisioned using advanced nanomaterials and will likely accelerate healthcare diagnosis, treatment, and monitoring. In addition, it seems that biosensors based on nanomaterials will also attract more attention in other fields such as food safety and environmental analysis.

It is hoped that this review will help researchers to achieve new innovative compounds using luminescent metal complexes, functionalized metal nanoparticles, nanocomposite materials and other biomolecules to produce and develop robust, sensitive and reliable platforms for early detection of biomarkers as well as other critical target analytes. In this way, it has an effective role in the progress and development of inorganic medicinal chemistry.

1. REFERENCES

[1] Porter, KA. "Effect of homologous bone marrow injections in x-irradiated rabbits". British Journal of Experimental Pathology. 1957. 38 (4): 401–412.

[2] Basu, PK., Miller, I., Ormsby, HL. "Sex chromatin as a biologic cell marker in the study of the fate of corneal transplants". American Journal of Ophthalmology, 1960. 49 (3): 513-515.

[3] Biomarkers Definitions Working Group. "Biomarkers and surrogate endpoints, Clinical Pharmacology and Therapeutics (Review). 2001. 69 (3): 89-95.

[4] McCarthy, JF, Shugart LR, 2018. Biological Markers of Environmental Contamination. Biomarkers of Environmental Contamination. Pp 3–14, CRC Pres.

[5] Depledge, MH., 2020. The Rational Basis for the Use of Biomarkers as Ecotoxicological Tools. Nondestructive Biomarkers in Vertebrates. pp. 271–295. 1st Edition, Taylor& Francis, CRC Press.

[6] Van, GCA., Van, BTC., Incorporation of the biomarker concept in ecotoxicology calls for a redefinition of terms. Ecotoxicology, 1996. 5 (4): 217–225.

[7] Kyle, S., & Jorge, A T. What are biomarkers? Current Opinion in HIV and AIDS, 2010. 5 (6): 463–466.

[8] Lmar, MB., Joseph, M., Michael, R., Giovanni N., et al, Traditional and Digital Biomarkers: Two Worlds Apart? Digit Biomark, 2019. 3:92–102.

[9] Hirsch, MS., Watkins, J. A Comprehensive Review of Biomarker Use in the Gynecologic Tract Including Differential Diagnoses and Diagnostic Pitfalls. Advances in Anatomic Pathology, 2020. 27 (3): 164–192.

[10] Jeffrey, KA., Biomarkers and surrogate endpoints. British Journal of Clinical Pharmacology, 2001. 59:5 491–494.

[11] Marc, B., Stefan, M., Daniel, JS., Axel, G., et al. Integrating biomarkers in clinical trials. Expert Review of Molecular Diagnostics, 2011. 11(2): 171–182.

[12] Gagné, F., Blaise, C., Costan, G., Gagnon, P., Chan HM. Biomarkers in zebra mussels (Dreissena polymorpha) for the assessment and monitoring of water quality of the St Lawrence River (Canada). Aquatic Toxicology, 2000. 50 (1–2): 51–71.

[13] Dik, LM., Chun, W., Guodong, L., Chung, H L, Group 8–9 Metal-Based Luminescent Chemosensors for Protein Biomarker Detection. Journal of Analysis and Testing, 2018, 2:77–89.

[14] LI, G., Long-lived iridium(III) complexes probes for luminescent detection of protein biomarkers and their activity, Doctor of Philosophy in Biomedical Sciences, Institute of Chinese Medical Sciences, University of Macau. 2020. 24 pages.

[15] Christine, FM., Andrew, GK., Carson, PM., Kelly, A., Richardson, and David W. Wright. Inorganic Complexes and Metal-Based Nanomaterials for Infectious Disease Diagnostics. Chemical Review, 2019. 119(2): 1456–1518.

[16] Richard, M. Biomarkers: Potential Uses and Limitations, NeuroRx. 2004. 1(2):182-188.

[17] Alyssa, BC., Chenxia MG., Jennifer RF., Stacey NB, et al, Nanoparticle Probes for the Detection of Cancer Biomarkers. Cells and Tissues by Fluorescence. Chemical Review, 115(19):10530-10574.

[18] Brian, R M & John, A B. Biomarkers and imaging: physics and chemistry for noninvasive analyses. Bioanalysis, 2009. 1(2): 321–356.

[19] Jianglan, L., Zhirui, Y., Long, W., Yumei, H., et al, Metabolite biomarkers of type 2 diabetes mellitus and pre-diabetes: a systematic review and meta-analysis. BMC Endocrine Disorders, 2020. 20:174-191.

[20] Thaddeus, JW., Edward, HW., Gary, RW., & Carolyn JA. Coordinating Radiometals of Copper, Gallium, Indium, Yttrium, and Zirconium for PET and SPECT Imaging of Disease. Chemical Review, 2010. 110: 2858–2902.

[21] Lauren, ES., & Chris, O., Medicinal Inorganic Chemistry Approaches to Passivation and Removal of Aberrant Metal Ions in Disease. Chemical Review, 2009. 109:4885–4910.

[22] Downing, GJ., Biomarkers and surrogate endpoints. Clinical Pharmacology & Therapeutics, 2001. 69:89-95.

[23] K. Koteshwara R., Harshad, B., Moru, S., Kotagiri, Y G., et al, Recent Trends in Electrochemical Sensors for Vital Biomedical Markers Using Hybrid Nanostructured Materials. advanced science, 2020. 7: 1902980-1903027.

[24] Aizpurua, OO, Sastre T J, Falcon-PJ.M, Williams C., et al. Mass spectrometry for glycan biomarker discovery. Trends in Analytical, Chemistry, 2018. 100:7-14.

[25] Cathy, S C., Heather. M H., Nebiat., S, Sandrine, HM., and Silvia, SJ. Radiometals for Combined Imaging and Therapy. Chemical Review, 2013, 113(2): 858-883.

[26] Eduardo, T., Gregor, W., Werner, P., The diagnosis of Parkinson's disease. Lancet Neurol, 2006. 5: 75–86.

[27] Eeva, LK., F-18 Labeling Synthesis, Radio Analysis and Evaluation of a Dopamine Transporter and a Hypoxia Tracer, University of Helsinki, Academic Dissertation, 2007. 63 pages..

[28] Halina A and Beata B P, Raman Imaging in Biochemical and Biomedical Applications. Diagnosis and Treatment of Breast Cancer, Chemical Review. 2013, 113, 8:5766–5781

[29] Sunil, KA., & Shekhar, B. Lung Cancer and Its Early Detection Using Biomarker-Based Biosensors. Chemical Review, 2011. 111: 6783–6809.

[30] Feiyun, C., Zhiru, Z., & Susan Z, Review-Measurement and Analysis of Cancer Biomarkers Based on Electrochemical Biosensors. Journal of The Electrochemical Society, 2020. 167:037525.

[31] Bradley J. Schwehr · David Hartnell, · Massimiliano Massi · Mark J. Hackett, Luminescent Metal Complexes as Emerging Tools for Lipid Imaging. Topics in Current Chemistry, 2022. 380:46-86.

[32] Kenneth, KWL., Alex, WTC., & Wendell, HTL., Applications of luminescent inorganic and organometallic transition metal complexes as biomolecular and cellular probes. Dalton Transactions, 2012. 41: 6021–6047.

[33] Tikum, FA., Gyoungmi, K., Ha, YJ., Juyoung, Y., Jinheung, K., Diiridium(III) Complexes: Luminescent Probes and Sensors for G- Quadruplex DNA and Endoplasmic Reticulum Imaging. New Journal of Chemistry, 2017. 41:377-386.

[34] Dik, LM., Hong, ZH., Daniel, SHC, Chun, YW., Chung-Hang Leung, A Colorimetric and Luminescent Dual-Modal Assay for Cu(II) Ion Detection Using an Iridium(III) Complex. PLOS ONE, 2014. 9(6): e99930- e99937.'

[35] Daniel, H., Luminescent d6 metal complexes for biomarker detection, Literature Seminar, University Illinois Urbana Champaign, United States, 2016. 4 October, 1-3.

[36] Wanhe, W., Lihua, L., Ke, JW., Jinshui, L., et al, Long-lived iridium(III) complexes as luminescent probes for the detection of periodate in living cells. Sensors and Actuators B: Chemical, 2019, 288: 392-398.

[37] Zonglun, L., Kuo, G., Beng, W., Hui, Y., et al. A dinuclear ruthenium(II) complex as turn-on luminescent probe for hypochlorous acid and its application for in vivo imaging. Scientific Reports, 2016. 6: 29065- 29070.

[38] Dik, LM., Modi, W., Chenfu, L., Xiangmin, M., et al. Metal complexes for the detection of disease-related protein biomarkers. Coordination Chemistry Reviews, 2016. 324: 90–105.

[39] Seo, YK., Hoon, JK., & Jong, IH., Electrochemiluminescent chemodosimetric probes for sulfide based on cyclometalated Ir(III) complexes. RSC Advances, 2017. 7:10865-10868.

[40] Tian, X., Xiao, L., Shen, Y., Luo, L., et al. A combination of super-resolution fluorescence and magnetic resonance imaging using a Mn(II) compound. Inorganic Chemistry Frontiers, 2019. 6(10):2914–2920.

[41] Kenneth, KWL., Wai, KH., Chi, KC., Keith, HKT, et al. Biological labelling reagents and probes derived from luminescent transition metal polypyridine complexes. Coordination Chemistry Reviews, 2005, 249: 1434–1450.

[42] Kenneth Kam-Wing Lo, Alex Wing-Tat Choi and Wendell Ho-Tin Law, Applications of luminescent inorganic and organometallic transition metal complexes as biomolecular and cellular probes, 2012,

[43] Heather, D S., Nancy, BT., Stacy, LT., & Kirk, SS, Unusual Photophysics of a Rhenium(I) Dipyridophenazine Complex in Homogeneous Solution and Bound to DNA. Journal of the American Chemical Society, 1995. 117: 7119 –7128.

[44] Vivian, WWY., Kenneth, KWL., Kung, KC., & Richard, YCK., Deoxyribonucleic acid binding and photocleavage studies of rhenium(I) dipyridophenazine complexes. Journal of the Chemical Society, 1997. 2067 – 2072.

[45] Wenzhu Zhang, Dan Zhao, Run Zhang,a Zhiqiang Ye, Guilan Wang, Jingli Yuan* and Mei Yang, ruthenium(II) complex based turn-on electrochemiluminescence probe for the detection of nitric oxide, 2011,

[46] Run, Z., Xiaojing, Y., Zhiqiang, Y., Guilan, W., et al, Turn-on Luminescent Probe for Cysteine/ Homocysteine Based on a Ruthenium(II) Complex. Inorganic Chemistry, 2010. 49: 7898–7903.

[47] Hongxing, L., Xiaoming, Z., Qi, S., & Da, X., Paper-based electrochemiluminescence sensor for highly sensitive detection of amyloid-β oligomerization: Toward potential diagnosis of Alzheimer's disease. Theranostics, 2018. 8(8): 2289-2299.

[48] Sanjoy, KS., Bhaskar, S., Romita, T., Kripamoy, A., and Snehadrinarayan, K., Ruthenium(II) Complex-Based Luminescent Bifunctional Probe for Ag+ and Phosphate Ions: Ag+-Assisted Detection and Imaging of RNA. Inorganic Chemistry, 2017. 56(3): 1249–1263.

[49] Xiangjun, M., Rui, T., Changqing, Y., Mei, JL., Fengfu, F. Colorimetric and Photoluminescent Probes Based on Iridium(III), Complexes for Highly Selective Detection of Homocysteine. 2022. 14 Pages, Available at: https://ssrn.com/abstract=4117339.

[50] Wanhe, W., Jianhua, L., Sang, CN., Dik, LM., et al. Affinity-Based Luminescent Iridium(III) Complexes for the Detection of Disease-Related Proteins. Inorganics, 2022. 10 (11):178-195.

[51] Taemin Kim and Jong-In Hong, Photoluminescence and Electrochemiluminescence Dual-Signaling Sensors for Selective Detection of Cysteine Based on Iridium(III) Complexes. ACS Omega, 2019. 4(7): 12616–12625.

[52] Phyllis, KMS., Dik, LM., & Chi, MC. Luminescent cyclometalated platinum(II) complexes with amino acid ligands for protein binding. Chemical Communications, 2005. 8: 1025–1027.

[53] Dik, LM., Hong, ZH., Ka, HL., Daniel, SHC., & Chung, HL. Bioactive Luminescent Transition-Metal Complexes for Biomedical Applications. Angewandte Chemie International Edition, 2013. 52: 2-19.

[54] Jawad, A., Balayeshwanth, RV., Phillipe, JCR., Nathan WL. Guanidinium-modified phthalocyanines as high-affinity G-quadruplex fluorescent probes and transcriptional regulators. Angewandte Chemie International Edition, 2009, 48: 9362 – 9365..

[55] Dien, NT., Nhung, NT., Anh, TV., Thuong, QT., et al, 2021. Pyridine dicarboxylate-Tb(III) Complex-Based Luminescent Probes for ATP Monitoring. Journal of Analytical Methods in Chemistry, 2021:7 pages

[56] Yafeng Zhao,Yanhong Xu, Bing Xu,c Peipei Cen, Weiming Song, Lijuan Duana and Xiangyu Liu, 2020

[57] Thorfinnur Gunnlaugsson, Andrew J. Harte, Joseph P. Leonard a & Mark Nieuwenhuyzen, The Formation of Luminescent Supramolecular Ternary Complexes in Water: Delayed Luminescence Sensing of Aromatic Carboxylates Using Coordinated Unsaturated Cationic Heptadentate Lanthanide Ion Complexes, 2014,

[58] Onur, A., Oleksandr, R., Sayo, OF., Weihua, W., et al. Lanthanide complexes as fluorescent indicators for neutral sugars and cancer biomarkers. Applied Biological Sciences, 2006. 103 (26): 9756-9760.

[59] Jorge H.S.K. Monteiro, Fernando A. Sigoli, and Ana de Bettencourt-Dias, 2017

[60] Lucas, AL., Ximei, Q., & Shuming, N., SERS Nanoparticles in Medicine: From Label-Free Detection to Spectroscopic Tagging, Chemical. Review. 2015. 115, 19:10489–10529.

[61] Chen. F., Huiling, L., Jilin, Y., Heming, G., & Tu, Y. Progress of the Electrochemiluminescence Biosensing Strategy for Clinical Diagnosis with Luminol as the Sensing Probe, ChemElectroChem, 2017. 4:1587-1593.

[62] Maryam, S., Parham, N., Roghayeh, A., The application of nanoparticles in diagnosis and treatment of breast cancer: a review article. Pajouhan Scientific Journal, 2015. 13(2):1-12.

[63] Linan Zhang & Chunchuan Gu & Jiajun Wen & Guangxian Liu & Hongying Liu & Lihua Li, Recent advances in nanomaterial-based biosensors for the detection of exosomes, 2021,

[64] Shiyu, Z., & Yang, L. Recent Progress of Novel Electrochemiluminescence Nanoprobes and Their Analytical Applications. Frontiers in Chemistry, 2021. 8: 626243- 626249.

[65] Saeideh H, An overview of the diagnostic applications of nanostructures, 16th National Congress of Biochemistry & 7th International Congress of Biochemistry & Molecular Biology, Tehran. Iran., 9 November. 2020.

[66] John, WK., & Jae J L. Photoluminescent Metal Complexes and Materials as Temperature Sensors-An Introductory Review Chemosensors, 2021. 9:109-120.

[67] Marina Martínez-Carmona, Yurii Gun'ko and María Vallet-Regí, ZnO Nanostructures for Drug Delivery and Theranostic Applications. Nanomaterials (Basel). 2018, 23;8(4):268.

[68] Xuefeng Tang, Zhao Wang, Feng Wei, Wei Mu and Xiaojun Han, Recent Progress of Lung Cancer Diagnosis Using Nanomaterials, Crystals, 2020, 11:24-35

[69] Hadi, ZZ., Asghar, TK., Amirhassan, A., Mehdi, S., et al. Nanotechnology and Pediatric Cancer: Prevention. Diagnosis and Treatment, Iranian Journal of Pediatric Hematology and Oncology, 2015. 5(4):233-248.

[70] Wu, XY., Liu, HJ., Liu, JQ., Haley, KN., et al. Immunofluorescent Labeling of Cancer Marker Her2 and Other Cellular Targets with Semiconductor Quantum Dots. Nature Biotechnology, 2002, 21:41-46.

[71] Song, EQ., Hu, J., Wen, CY., Tian, ZQ., et al, Fluorescent-Magnetic-Biotargeting Multifunctional Nanobioprobes for Detecting and Isolating Multiple Types of Tumor Cells. ACS Nano, 2011, 5:761-770.

[72] Cheng, L A., Yang, K., Shao, M W., Lee, S T., and Liu, Z A. Multicolor in Vivo Imaging of Upconversion Nanopaticles with Emissions Tuned by Luminescence Resonance Energy Transfer. Journal of Physical Chemistry C, 2011. 115: 2686-2692.

[73] Chen, XS., Lan, JM., Liu, YX., Li, L., et al. A paper supported aptasensor based on up-conversion luminescence resonance energy transfer for the accessible determination of exosomes. Biosensors and Bioelectronics, 2018. 102: 582-588.

[74] Minho, K., Jung, HL., & Jwa, M N, Plasmonic Photothermal Nanoparticles for Biomedical Applications, Advanced Science. 2019. 6: 1900471, 1900493.

[75] Yingjie, Y., Datao, T., Yunqin, Z., Peng, Z., and Xueyuan, C., Recent advances in design of lanthanide-containing NIR-II luminescent nanoprobes. iScience, 2021. 24 (2):102062-102081.

[76] Ilkka H & Ville L, Progress in Lanthanides as Luminescent Probes. Journal of Fluorescence, 2005, 15 (4): 529-542.

[77] Cao, Z., Shu, Y., Qin, H., Su, B., & Peng, X. Quantum dots with highly efficient, stable, and multicolor electrochemiluminescence. ACS Central Science, 2020. 6: 1129-1137.

[78] Elnaz, B., Legha, A., Khalil, A., Seyed Mohammad, T., et al. Silica -magnetic inorganic hybrid nanomaterials as versatile sensing platform. Nanomedicine Journal, 2020. 7(3): 183-193.

[79] Yong, C., Jiaxin, L., Luyao, Y., Miaomiao, L., et al, Design and Application of Electrochemical Sensors with Metal–Organic Frameworks as the Electrode Materials or Signal Tags Nanomaterials, 2022. 12: 3248-3283.

[80] Shijun, W., Shu, Z., Ziqi, K., Yidan, C., et al. Recent advances and future prospects of the potential resolved strategy in ratiometric, multiplex, and

multicolor electrochemiluminescence analysis, Theranostics, 2022. 12(15): 6779-6808.

[81] Sanghyuck, L., Chul, SP., & Hyeonseok, Y. Nanoparticulate Photoluminescent Probes for Bioimaging: Small Molecules and Polymers International. Journal of Molecular Sciences, 2022, 23: 4949.

Applied *Nanomaterials and smart Polymers,*
Online ISSN: 2981-0434
Vol. 1, No. 3

ANSP

The Study on the Welding Area of Metal Using Both Optical and Electron (SEM) Microscopes

Seyed Alireza Mousavi Shirazi[1 *], Ali Wail Salman Sangoor[1]

[1]Department of Physic, South Tehran Branch, Islamic Azad University, Tehran, Iran.

ABSTRACT

To better study the performance of welding on metal and treating it with an alloy, considering the area of metal welding from the metallurgical point of view, and the analysis of nanostructural characteristics is of great importance. In this research, the samples of stainless steel were taken into consideration by both optical and electron microscopes (SEM) for the sake of nanostructural consideration and diagnosis of the corrosion type. Thus, a cycle of annealing operation at 300 ºC and spanning one hour, which is an appropriate cycle to achieve the desired characteristics of corrosion and mechanical properties for the welded stainless steel, was applied. The results of both EDS analysis and SEM images showed that in the area affected by welding and weld nuggets, carbide sintering is formed, and the majority of observed phases amid granules stem from the formation of various metallic carbides like ferrite carbide, chrome carbide, and niobium carbide.

Keywords

Corrosion; Electron Microscope; Metal; Optical Microscope; Welding area.

1. Introduction

In some research, the sharpie hit has been used to consider high-strength micro-alloy steel resistance against the break. Also, to accurately consider the nanostructures before and after the thermal operations, both optical and electron (SEM) microscopes have been applied [1, 2]. According to the results obtained by research, the optimal braking energy is related to the irradiated cycle and its reheat at temperatures of 950 ºC and 650 ºC, respectively [3, 4].

In this thermal cycle, the final nanostructure includes pearlite, multi-faceted ferrite, and many metal oxide impurities [5]. The broken surface indicates that the pearlite nanostructure and the multi-faceted ferrite have a softer break than a pearlite-ferrite sample.

In a sample having the maximum break energy, the minimum consistency compared to other heated samples was observed [6]. Also, in some research, the effects of surface conditions on the resistance of both corrosion and sulfide-tensile have been discussed for Steel-316L [7]. This research aims to study surface devastation that stems from part machining and the presence of thermal-colored oxides because of the welding operation. From the images of EBSD and SEM taken from the samples, it is concluded that there has been nanostructure in samples adjacent to their surfaces in advance of bending, which can be attributed to surface finishing [8]. The accurate

* Corresponding Author Email: a_moosavi@azad.ac.ir

study of these images and SSRT corrosion tests shows that in machining failures, the cavities tend to be more concentrated in non-metallic inclusions for the spread [9]. The research results have shown that the smoother the surface, the more cavities [10]. Researchers have also considered the effect of the thermal-colored oxide being pitted. The results showed that the presence of this thermal color oxide causes the density of cavities to increase, and it can also cause crack advancement [11].the presence

These researchers suggested that the crack starts because of the alloy element evacuation in some regions.

In this research, the aim is a microscopic consideration of the effect of stainless-steel welding area on nonstructural characteristics and granulation of that area [12, 13].

2. Materials and Methods

2.1. A welded sample under two-hour thermal operation

In this research, the images of both optical and electron (SEM) microscopes, along with the acquired images of different welding areas, have been taken into consideration. As shown in Fig. 1, the welding area is divided into three main sections: the weld nugget, the area affected by welding, and the base metal.

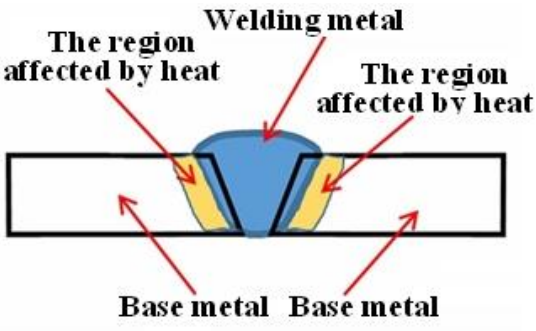

Fig. 1. The division of various areas of welding

In Fig. 2, the images extracted by optical and SEM microscopes have been illustrated for triple welding areas without thermal operation. In this investigation, a cycle of an annealing operation at 300 ºC and spanning one hour, a proper cycle to achieve the desired mechanical and corrosion characteristics, was used for stainless steel in the welding operation.

The images by optical microscopes showed that the stainless steel includes ferrite granulation with distributed particles in a steel matrix. This structure also has an austenite background with ferrite, and the existence of this structure in stainless steel granulation is due to the steel fabrication process during its rolling process, which is observable in welding the base metal. The images from the optical microscope showed no significant changes were observed in granulation or the structure of the base metal during the thermal operation. However, the thermal operation has little effect on the change of grain growth in both the areas affected by welding and the welding nuggets. In Figs. 2-5, the images of the metallographic and nanostructure of triple areas have been illustrated for two, four, and six hours of thermal operation. Considering the results, they showed that through the thermal operation, the ferrite grains have grown axially. Hence, this grain growth is an essential factor in decreasing tensile concentration in the area affected by welding, and it causes a decrease in the escalation of the melting crack. The analysis of the nanostructure images showed that the growth of the grains in the base metal region is axial. Still, the effects of the thermal operation have caused the grains' growth and their directions in the welding nugget area to change, and this has caused the boundaries of the grains to spread. Taking into consideration the images from the SEM microscopes, it is recognized that the grain growth is axially in the state without thermal operation in a way that, through increasing the duration of thermal operation (specifically in the welding nugget area), this axial growth has been limited, and the boundary of grains has spread throughout the area of welding nugget and the area affected by welding on the other side, the effect of the thermal operation on the area of welding nugget and the area affected by

welding has caused to reduce the size of granulation in these areas.

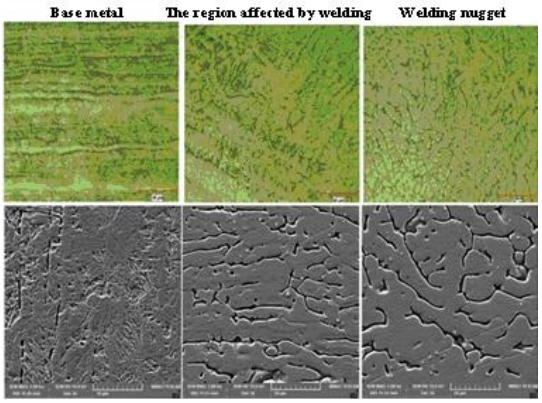

Fig. 2. The images of both optical and SEM microscopes for different welding areas in the condition of non-thermal operation

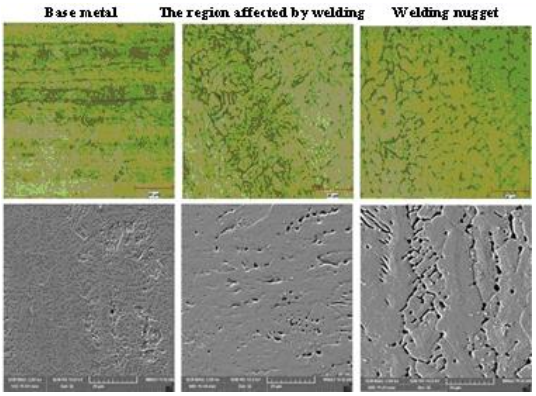

Fig. 3. The images of both optical and SEM microscopes for different welding areas in the condition of 2-hour thermal operation

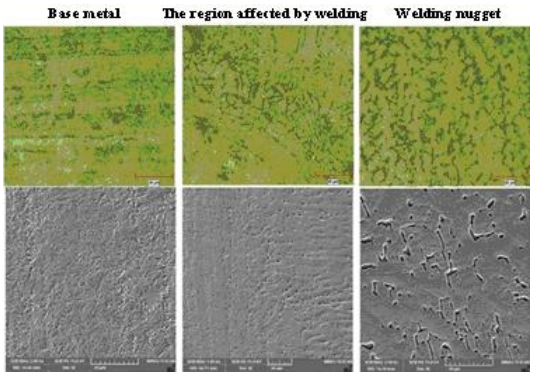

Fig. 4. The images of both optical and SEM microscopes for different welding areas in the condition of 4-hour thermal operation

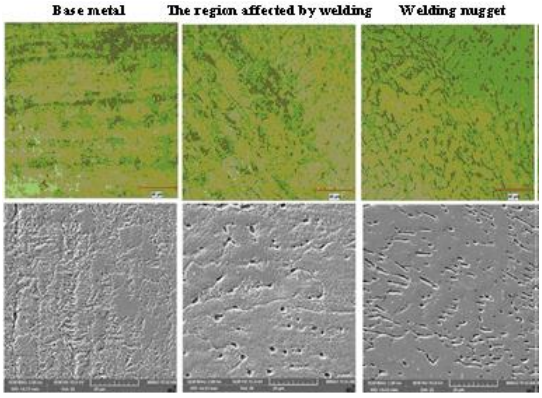

Fig. 5. The images of both optical and SEM microscopes for different welding areas in the condition of 6-hour thermal operation

The analysis of the elements existing in phase A shows that most of the volumes of constituent elements of this phase are niobium, iron, and chrome, which have formed the sediment of Fe-Nb-Cr. The existence of niobium in phase A stems from melting down the welding electrode. One of the factors that can form carbides of various elements in phase A is the existence of the iron element, which raises the probability of Cr_3C_2, NbC, and Fe_3C. Besides, since phase A has been formed between the stainless steel grains, this phase may cause corrosion between the above-mentioned carbide grains. The mass percentage of niobium element in phases B and C was less than in phase A, so in these phases, most of the volumes of the constituent elements are iron, carbon, and chrome, and the existence of these three elements raises the probability of the carbide formation of chrome and iron. Analysis of the elements existing in phase B shows that the major consistent elements in this phase include carbon, chrome, and iron, in a way that, because of the presence of these elements in phase B, the probability of carbide sediment formation of chrome and iron is increased. Phase C also included the elements of carbon, titanium, oxygen, chrome, manganese, and nitrogen, such that the presence of the oxygen element in this phase indicates corrosion, and oxygen forms about 42% of the constituent elements of this phase. This volume of oxygen can cause the formation of metal oxides such as

TiO_2, Cr_2O_3, and MnO in phase C. In Fig.6, the microscopic image of a welding nugget area has been shown for a welded sample under 2-hour thermal operation.

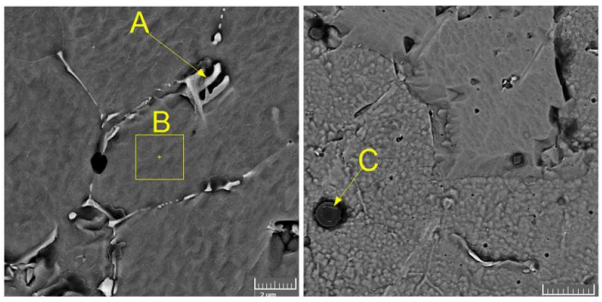

Fig. 6. The SEM image of the welding nugget area for a welded sample under 2-hour thermal operation

As shown in Figure 6, the diameter of the corrosion area is almost 1 mm. Figure 7 shows the SEM image and quantitative analysis of the elements for the area affected by welding for a welded sample under 2-hour thermal operation.

Nitrogen, sulfur, chrome, and titanium are the primary constituent elements of phase D, and the existence of these elements may raise the probability of the presence of both chromium and titanium sulfides.

Phase F (like phase D) also has similar element components; the only difference is that it has the highest percentage of sulfur and titanium.

The percentage of iron element existing in phase D is higher than that of phase F, which might be because of the greater volume of corrosion in phase F. Also, the signs of corrosion in the welding nugget areas were not observed, and this was while in the areas affected by the welding, there were signs of corrosion stemming from H_2S gas in the grain boundary. In the welding nugget area, because of a higher temperature, the metal particles existing in this area are easily dissolved together. Conversely, due to metal particles being molten and their complete dissolution together, granulation in this welding nugget area is tinier. This issue causes an increase in the resistance of the welding nugget area to corrosion rather than the area affected by welding. Considering the constituent elements of phase D, it shows that in this area, there is a probability of the sediments of both chromic carbide and iron carbide because of the high volume of iron, carbon, and chrome. In the area affected by welding, metal elements do not dissolve well because of the low temperature, which may raise the probability of intergranular sediment formation.

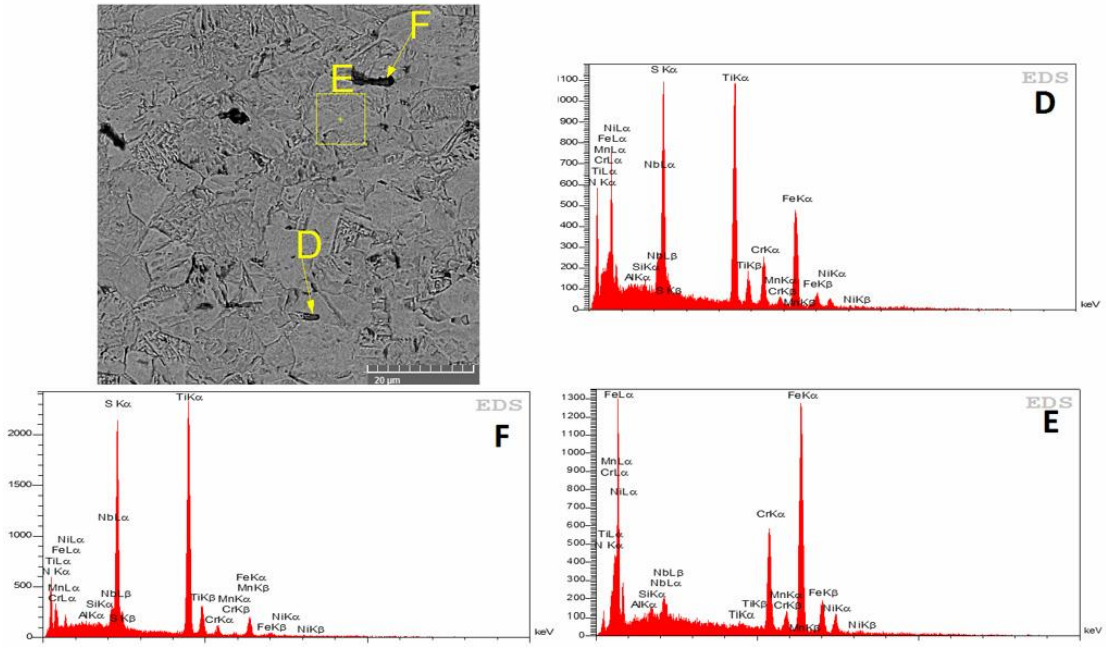

Fig. 7. The SEM image and quantitative analysis results of the elements for the area affected by welding for a welded sample under 2-hour thermal operation

3. Results

In Table 1, the results of element analysis have been shown for phases A, B, and C.

Table 1. The analysis of element weight percentage for the welding nugget area within a 2-hour thermal operation

Phase	Nb	Ni	Fe	Mn	Cr	Ti	Si	Al	O	N
A	29.24	2.4	16.73	0.15	6.52	0.09	0.48	0.3	0.0	10.44
B	2.97	9.07	57.62	1.27	15.77	0.0	0.68	0.06	0.0	1.58
C	2.59	0.2	1.9	10.0	6.35	18.6	0.45	2.15	42.06	9.83

According to the table above, most elements in phase A include carbon, niobium, iron, and nitrogen, respectively. Of course, the iron existing in this phase may be because the base metal is molten; niobium and nitrogen of this phase can also stem from the electrode being molten and dissolved with the welding melt. Table 2 presents the qualitative analysis of elements existing in phases E, D, and F.

Table 2. The qualitative analysis of elements' weight percentage in the phases E, D, and D for the area affected by welding for a welded sample under 2-hour thermal operation

Phase	Nb	Ni	Fe	Mn	Cr	Ti	S	Si	Al	N
D	3.17	1.92	19.92	0.0	5.52	17.84	6.33	0.28	0.18	14.57
E	2.51	7.42	64.62	0.29	15.70	0.28	0.0	0.41	0.05	1.98
F	2.66	0.26	5.44	0.0	1.62	32.18	10.69	0.18	0.16	19.37

In Figure 8, the maximum amount of bending resistance has been illustrated for the various samples.

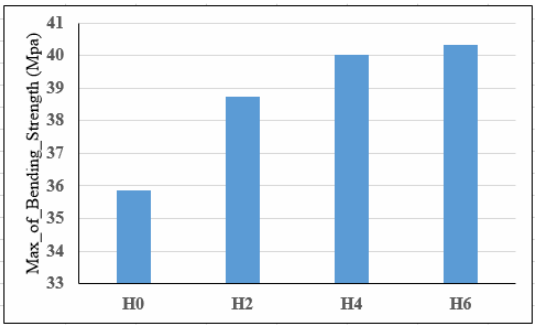

Fig. 8. The maximum amount of bending resistance for the welded samples under thermal operation

The results showed that in the case of not having thermal operation, the maximum resistance of bending for the samples is 35.86 MPa in a way that through doing thermal operations for two, four, and six hours at the temperature of 870 ºC, the amount of bending resistance will be 38.73 MPa, 40.02 MPa, and 40.33 MPa, respectively. The analysis of the bending test results showed that exerting two, four, and six hours of thermal operation at a temperature of 870 ºC causes the improvement of maximum bending resistance of the samples by 8%, 10.74%, and 11.17%, respectively. In Figure 9, the triple point bending test results are illustrated in the stress-strain curve for the various models of the welded samples under thermal operation. Considering the curve of stress-strain, it showed that because of thermal operation in the studied samples, the value of sample bending resistance increased, but the value of axial strain decreased. As shown in the metallographic images, after doing the thermal operation on the studied samples, the size of granulation became tinier in a way that this issue caused an improvement of the mechanical characteristics of the analyzed samples.

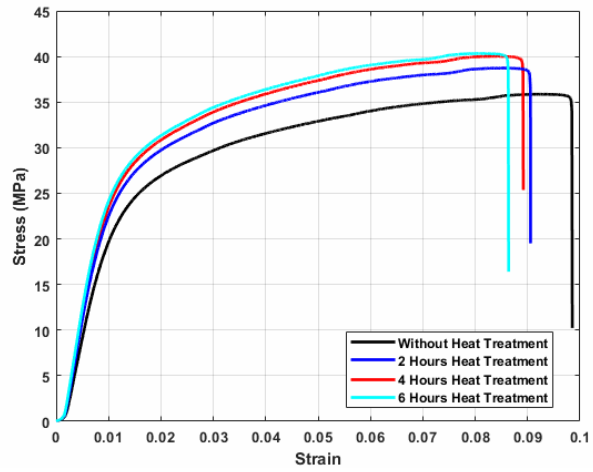

Fig. 9. The stress-strain curve of the triple-point bending test for the samples under thermal operation

The results of the uniaxial tensile test (in the stress-strain curve) and comparison of maximum tensile resistance have been shown in Figures 10 and 11 for the various samples under thermal operation.

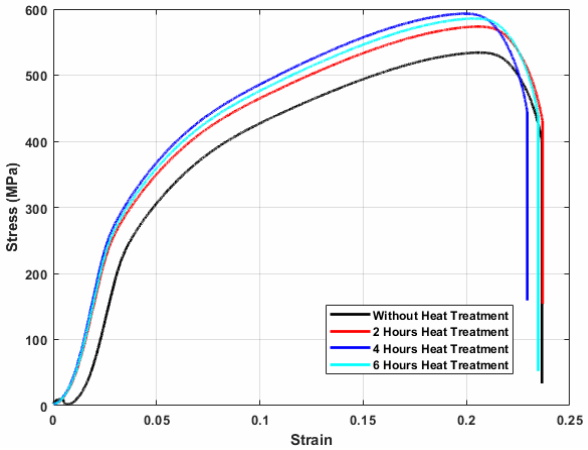

Fig. 10. The stress-strain curve of the tensile test for the samples under thermal operation

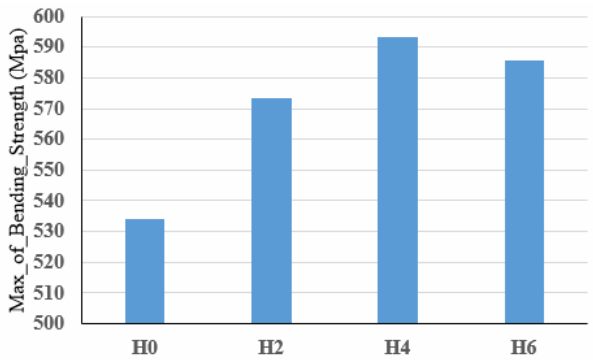

Fig. 11. The tensile resistance for the welded samples under various thermal operations

4. Conclusions

The stress–strain curves revealed that thermal treatment of welded stainless steel samples increased ultimate tensile strength while reducing axial strain. Metallographic analysis confirmed that thermal treatment refined the grain structure, contributing to improved tensile strength. However, the increased brittleness of the thermally treated microstructure corresponded with a reduction in axial elongation. Comparative analysis showed that the untreated sample exhibited a maximum tensile strength of 534.15 Pa, which increased by 6.86%, 9.93%, and 8.80% after 2, 4, and 6 hours of thermal treatment, respectively. Among these, the 4-hour thermal treatment produced the highest overall mechanical performance, including both tensile and bending resistance. While 4- and 6-hour treatments yielded similar mechanical enhancements, the marginal gain beyond 4 hours was less than 1%, indicating diminishing returns with extended treatment. EDS analysis and SEM imaging confirmed the formation of metal carbides—notably of iron, chromium, and niobium—in the heat-affected zone (HAZ) and weld nugget. Additionally, exposure to H_2S gas induced localized corrosion, although carbide precipitation remained the dominant microstructural change observed at grain boundaries.

References

[1] Sedighi, M., Shajari, Y., Razavi, S. H., Sabet, H., & Porhonar, M. (2021). The Effect of Post-Weld Heat Treatment (PWHT) on the Microstructure, Microhardness, and Sulphide Stress Corrosion Cracking (SSCC) of Ni-Base Superalloy IN625 Hot Wire TIG Cladding on AISI 4130 Steel. Protection of Metals and Physical Chemistry of Surfaces, 57(1), 113–120.

[2] Soares, C. G., Garbatov, Y., Zayed, A., & Wang, G. (2008). Corrosion wastage model for ship crude oil tanks. Corrosion Science, 50(11), 3095–3106. https://doi.org/10.1016/j.corsci.2008.08.035

[3] Zhou, P., Liang, J. M., Zhang, F., Wu, H. B., & Tang, D. (2015). Influence of chromium on corrosion behavior of low-alloy steel in cargo oil tank O2-CO2-SO2-H2S wet gas environment. Journal of Iron and Steel Research International, 22(7), 630–637. https://doi.org/10.1016/S1006-706X(15)30050-9

[4] Liu, B., Wei, X., Wang, W., Lu, J., & Ding, J. (2017). Corrosion behavior of Ni-based alloys in molten NaCl-CaCl2-MgCl2 eutectic salt for concentrating solar power. Solar Energy Materials and Solar Cells, 170, 77–86. https://doi.org/10.1016/j.solmat.2017.05.042

[5] Pešička, J., Kužel, R., Dronhofer, A., & Eggeler, G. (2003). The evolution of dislocation density during heat treatment and creep of tempered martensite ferritic steels. Acta Materialia, 51(16), 4847–4862. https://doi.org/10.1016/S1359-6454(03)00355-4

[6] Totten, G. E. (Ed.). (2006). Steel heat treatment: Metallurgy and technologies. CRC Press. https://doi.org/10.1201/NOF0849384523

[7] Hinds, G., Wickström, L., Mingard, K., & Turnbull, A. (2013). Impact of surface condition on sulphide stress corrosion cracking of 316L stainless steel. Corrosion Science, 71, 43–52. https://doi.org/10.1016/j.corsci.2013.01.027

[8] Cabrera-Sierra, R., Garcıa, I., Sosa, E., Oropeza, T., & González, I. (2000). Electrochemical behavior of carbon steel in alkaline sour environments measured by electrochemical impedance spectroscopy. Electrochimica Acta, 46(4), 487–497. https://doi.org/10.1016/S0013-4686(00)00567-3

[9] Sharma, R. C. (2003). Principles of heat treatment of steels. New Age International.

[10] Velázquez, J. C., Caleyo, F., Cabrera-Sierra, R., Teran, G., Hernandez-Sanchez, E., Capula-Colindres, S., Herrera-Hernández, H., & Ortiz-Herrera, C. C. (2018). A Bayesian approach for estimating the thinning corrosion rate of steel heat exchangers in hydrodesulfurization plants. Advances in Materials Science and Engineering, 2018, 1–13. https://doi.org/10.1155/2018/6973052

[11] Chen, Y. Y., Liou, Y. M., & Shih, H. C. (2005). Stress corrosion cracking of type 321 stainless steels in simulated petrochemical process environments containing hydrogen sulfide and chloride. Materials Science and Engineering: A, 407(1–2), 114–126. https://doi.org/10.1016/j.msea.2005.07.011

[12] Moura, V., Kina, A. Y., Tavares, S. S. M., Lima, L. D., & Mainier, F. B. (2008). Influence of stabilization heat treatments on microstructure, hardness, and intergranular corrosion resistance of the AISI 321 stainless steel. Journal of Materials Science, 43(2), 536–540. https://doi.org/10.1007/s10853-007-2072-7

[13] TATSUKAWA, I., & ODA, A. (1972). Some metallurgical observations on the heating of explosive austenitic stainless clad steel. Transactions of the Japan Welding Society, 3(1), 48–58.

Applied *Nanomaterials and smart Polymers,*
Online ISSN: 2981-0434
Vol. 1, No. 3

ANSP

Synthesis and Characterization of Cellulose Nanocrystal-Grafted Poly (2-dimethylaminoethyl methacrylate) via RAFT Polymerization for pH-Responsive Nitrate Removal from Aqueous Solutions

Mojtaba Azizi[1*] , Milad Aghazadeh-Bonab[2] , Seyed Mahdi Saedi[3]

[1] Faculty of Chemistry and Chemical Engineering, Malek Ashtar University of Technology, P.O. Box 16765-3454,Tehran, Iran.

[2] Department of Polymer Engineering and Color Technology, Amirkabir University of Technology, P.O. Box 15875-4413, Tehran, Iran

[3] Faculty of Industrial Engineering, Sharif University of Technology, Tehran, Iran

ABSTRACT

This study focuses on the synthesis and characterization of poly(2-dimethylaminoethyl methacrylate) (PDMAEMA) grafted onto cellulose nanocrystals (CNC) using reversible addition-fragmentation chain transfer (RAFT) polymerization.1 The successful grafting of PDMAEMA onto CNC was confirmed using Fourier-transform infrared (FTIR) spectroscopy and thermogravimetric analysis (TGA).23 The resulting material, CNC-g-PDMAEMA, demonstrated pH-responsive characteristics consistent with the protonation/deprotonation behavior of the PDMAEMA tertiary amine groups.2 Preliminary adsorption studies indicated that nitrate uptake is enhanced under acidic conditions (pH < 6), attributed to increased electrostatic interactions between the protonated PDMAEMA grafts and nitrate anions. However, quantitative assessment of the adsorption capacity requires further investigation using validated analytical methods and standard adsorption protocols. This research highlights the potential of RAFT polymerization for preparing CNC-based stimuli-responsive materials 40 for environmental applications, although rigorous quantification of adsorption performance and regeneration capabilities is needed to fully establish its efficacy for water purification.

Keywords: Cellulose Nanocrystals (CNC), Poly(2-dimethylaminoethyl methacrylate) (PDMAEMA), RAFT Polymerization, Graft Polymerization, Nitrate Removal, Adsorption, Stimuli-Responsive Polymers.

1-Introduction

Water contamination by inorganic anions, notably nitrate (NO_3^-), represents a significant global environmental challenge, particularly prevalent in agricultural and industrial regions.41 Elevated nitrate concentrations in water sources pose severe health risks, including methemoglobinemia (especially in infants, often termed "blue baby syndrome") 51 and potential carcinogenic effects due to the formation of N-nitroso compounds.54 Furthermore, excess nitrate contributes to the eutrophication of surface waters, leading to ecological imbalances.49 Regulatory bodies like the World Health Organization (WHO) and the US Environmental Protection Agency (EPA) have set maximum contaminant levels for nitrate in drinking water, typically around 10-11.3 mg/L as nitrogen (NO_3^--N) or 45-50 mg/L as nitrate (NO_3^-).51 Conventional nitrate removal technologies, such as ion exchange, reverse osmosis, and biological denitrification, often face limitations including high operational costs, generation of secondary waste (e.g., concentrated brine from ion exchange regeneration), membrane fouling, or insufficient removal efficiency, particularly at

* Corresponding Author Email: azizi.m_58@yahoo.com

lower concentrations.23 Consequently, the development of efficient, cost-effective, and environmentally sustainable materials and methods for nitrate removal remains an active area of research.56

Building upon established expertise in developing adsorbent materials for wastewater treatment 49 and applying principles of green chemistry 13, this study investigates stimuli-responsive polymer adsorbents based on renewable resources. The use of cellulose nanocrystals (CNCs), derived from abundant biomass 86, aligns with green chemistry principles promoting sustainable materials.88

In recent years, stimuli-responsive polymers materials that undergo significant physicochemical changes in response to external triggers like pH, temperature, CO_2, or light—have garnered considerable interest for water treatment applications.40 These "smart" polymers can be designed as hydrogels, nanoparticles, or surface coatings for selective contaminant uptake and release.41 Controlled radical polymerization (CRP) techniques, such as nitroxide-mediated polymerization (NMP), atom transfer radical polymerization (ATRP), and reversible addition-fragmentation chain transfer (RAFT) polymerization, are frequently employed for synthesizing these materials.5 RAFT polymerization, in particular, offers versatility across a wide range of monomers and reaction conditions, including potentially greener solvent systems, and allows for precise control over polymer architecture (molecular weight, dispersity, block sequences) by mediating the polymerization through a thiocarbonylthio chain transfer agent.1

Cellulose nanocrystals (CNCs) are attractive substrates for modification due to their high specific surface area (typically 150–250 m^2/g), high aspect ratio, mechanical strength, renewability, and abundance of surface hydroxyl groups amenable to chemical functionalization.86 Grafting stimuli-responsive polymers onto CNCs can create hybrid nanomaterials with enhanced adsorption properties for water treatment.90 Poly(2-dimethylaminoethyl methacrylate) (PDMAEMA) is a well-known stimuli-responsive polymer exhibiting both pH and temperature sensitivity (Lower Critical Solution Temperature, LCST) in aqueous solutions.2 Its tertiary amine groups can be protonated at acidic pH (pKa ≈ 7.5), rendering the polymer cationic and enabling electrostatic interactions with anions like nitrate.2 Furthermore, PDMAEMA can respond to CO_2 sparging, which lowers the pH via carbonic acid formation, similarly inducing protonation and enhancing anion binding.51 Desorption can potentially be triggered by increasing the pH or temperature above the LCST, or by purging with an inert gas (like N_2) to remove CO_2.132

Prior research has explored CNCs functionalized with PDMAEMA-containing copolymers (synthesized via RAFT or ATRP) for nitrate removal.51 For instance, Abousalman-Rezvani et al. synthesized CNC-grafted copolymers of DMAEMA and coumarin via RAFT, demonstrating CO_2-triggered nitrate adsorption.51 They reported that higher PDMAEMA content led to increased adsorption capacity, although specific quantitative values require careful comparison considering experimental conditions.90 Another study by the same group used ATRP to graft similar copolymers, also showing CO_2-responsive nitrate uptake.51 These studies highlight the potential of CNC-PDMAEMA systems but often involve more complex copolymer structures or different polymerization techniques.

This study aims to synthesize CNC grafted with PDMAEMA homopolymer chains (CNC-g-PDMAEMA) using RAFT polymerization via a "grafting from" approach.15 The objectives are: (1) to successfully synthesize and characterize the CNC-g-PDMAEMA material using FTIR and TGA, (2) to investigate its pH-responsive behavior, and (3) to evaluate its potential for nitrate ion removal from aqueous solutions.

This work focuses on the RAFT synthesis of homopolymer grafts and provides foundational characterization and preliminary adsorption insights, contributing to the development of sustainable CNC-based adsorbents for environmental remediation.

2-Experimental

Materials

Microcrystalline cellulose (MCC, Avicel PH-101, Sigma-Aldrich, specified grade/particle size if available), sulfuric acid (H_2SO_4, Merck, specify concentration, e.g., 95-98%, ACS reagent grade), S-(thiobenzoyl)thioglycolic acid (RAFT agent, ≥98%, Sigma-Aldrich), 4-dimethylaminopyridine (DMAP, ≥99%, Sigma-Aldrich), N,N'-dicyclohexylcarbodiimide (DCC, 99%, Sigma-Aldrich), 2-(dimethylamino)ethyl methacrylate (DMAEMA, 98%, contains MEHQ inhibitor, Merck), azobisisobutyronitrile (AIBN, 98%, Sigma-Aldrich), sodium hydroxide (NaOH, ACS reagent, ≥97.0%, pellets, Merck), tetrahydrofuran (THF, anhydrous, ≥99.9%, inhibitor-free, Merck), methanol (ACS spectrophotometric grade, ≥99.9%, Merck), ethanol (absolute, ≥99.8%, Merck), and potassium nitrate (KNO_3, ACS reagent, ≥99.0%, Merck) were used. Deionized (DI) water (specify resistivity, e.g., 18.2 MΩ·cm, obtained from a Milli-Q system) was used throughout the experiments. DMAEMA monomer was purified by passing through a column of basic alumina (activated, basic, Brockmann I, Sigma-Aldrich) immediately before use to remove the inhibitor.77 AIBN was recrystallized twice from methanol prior to use.150 All other chemicals were used as received unless otherwise noted.

Preparation of Cellulose Nanocrystals (CNC)

CNCs were prepared by sulfuric acid hydrolysis of MCC following a modified literature procedure.87 Briefly, MCC (e.g., 10 g) was added to a preheated (45 °C) sulfuric acid solution (e.g., 100 mL of 64 wt% H_2SO_4 in DI water) under vigorous mechanical stirring. The hydrolysis was allowed to proceed at 45 °C for 1 hour. The reaction was quenched by adding a 10-fold excess of cold DI water. The resulting suspension underwent three cycles of centrifugation (e.g., 10,000 rpm, 15 min, 10 °C) and redispersion in DI water using probe ultrasonication (specify instrument, power, duration, e.g., 10 min per cycle, ensuring temperature control with an ice bath).18 After the final centrifugation, the suspension was neutralized by washing with dilute NaOH solution (e.g., 0.1 M) until the supernatant reached pH ~7, followed by washing with DI water until the conductivity of the supernatant was constant.18 The purified CNC suspension was then freeze-dried (specify conditions, e.g., pre-frozen at -80 °C, lyophilized at -50 °C, <0.1 mbar for 72 h) to obtain a white, fluffy solid.14

Synthesis of RAFT Agent-Functionalized CNC (CNC-CTA)

The RAFT agent, S-(thiobenzoyl)thioglycolic acid (here denoted as CTA), was attached to the CNC surface via esterification using DCC/DMAP coupling, adapted from reference.1 In a typical procedure, CNC (0.1 g, estimate surface hydroxyl moles if possible) was dispersed in anhydrous THF (15 mL) in a 50 mL round-bottom flask via ultrasonication (e.g., 15 min bath sonication). CTA (0.1 g, calculate moles), DCC (0.16 g, coupling agent, calculate moles), and DMAP (0.056 g, catalyst, calculate moles) were added sequentially. State molar ratios (e.g., [OH]::[DCC]:[DMAP]). The flask was sealed under a nitrogen atmosphere and immersed in an oil bath preheated to 40 °C. The reaction mixture was stirred magnetically for 3 days. After the reaction, the mixture was cooled, and the product was purified by repeated precipitation in cold methanol (e.g., 200 mL) followed by redissolution in THF (e.g., 10 mL) and centrifugation to remove DCC byproducts (dicyclohexylurea) and unreacted reagents. This purification cycle was repeated

three times. The final product (CNC-CTA) was dried under vacuum. (Describe how purity was confirmed, e.g., FTIR analysis showing disappearance of free CTA peaks, elemental analysis for sulfur content).

Synthesis of CNC-g-PDMAEMA via RAFT Polymerization

PDMAEMA chains were grafted from the CNC-CTA surface using RAFT polymerization ("grafting from" approach).1 CNC-CTA (0.1 g, estimate moles of CTA groups) was dispersed in anhydrous THF (specify initial volume, e.g., 5 mL) in a glass vial using ultrasonication (e.g., 20 min bath sonication). Purified DMAEMA monomer (7.5 mL, calculate moles), free CTA (S-(thiobenzoyl)thioglycolic acid, 0.002 g, explain purpose, e.g., potentially to mediate free polymer formation or improve control), AIBN initiator (0.01 g, calculate moles), and additional anhydrous THF (45 mL) were added sequentially. Calculate and state the target molar ratios [DMAEMA]:::. The vial was sealed with a rubber septum and deoxygenated by purging with dry nitrogen gas for 10 min while cooled in an ice bath. The vial was then placed in an oil bath preheated to 75 °C and stirred magnetically for 24 hours. Polymerization was terminated by cooling the vial rapidly (e.g., immersing in ice water) and exposing the contents to air. The product (CNC-g-PDMAEMA) was isolated and purified by precipitation into a large excess of a non-solvent (e.g., cold n-hexane), followed by centrifugation, washing with the non-solvent (3x), and drying under vacuum at room temperature. (State if monomer conversion was monitored, e.g., by ^{1}H NMR or gravimetry after sampling, or if the reaction was run for a fixed time). THF was chosen as the solvent based on its ability to disperse CNC-CTA and compatibility with the RAFT process as reported in reference 8, although alternative greener solvents like ethanol/water mixtures could be explored in future optimizations.114

3-Characterization

● Fourier-Transform Infrared (FTIR) Spectroscopy: FTIR spectra were recorded using a spectrometer equipped with an Attenuated Total Reflectance (ATR) accessory (e.g., diamond crystal). Spectra were collected in the range of 4000–400 cm^{-1} with a resolution of 4 cm^{-1} by averaging [Number, e.g., 32] scans. Dried powder samples were pressed firmly against the ATR crystal for analysis.23

● **Thermogravimetric Analysis (TGA):** TGA was performed using a thermogravimetric analyzer. Samples (typically 5–10 mg) were heated from 30 °C to 800 °C at a constant heating rate of under a nitrogen atmosphere (flow rate).23 Derivative thermogravimetric (DTG) curves were obtained by differentiating the TGA curves.

● **UV-Vis Spectroscopy (for Adsorption Study):** Nitrate concentrations were intended to be measured using a UV-Vis spectrophotometer. Measurements were performed using 1 cm path length quartz cuvettes. Note: The original method using 290 nm is non-standard for nitrate. Future studies should employ a validated method, such as the standard UV screening method measuring absorbance at 220 nm and correcting for organic interference at 275 nm 169, or alternative validated techniques like ion chromatography or colorimetric assays involving derivatization.23 Calibration curves should be generated using standard KNO_3 solutions in the relevant concentration range, and method validation (linearity, LOD, LOQ, interference checks) must be performed.

Adsorption Study

Batch adsorption experiments were conducted to evaluate the nitrate removal capability of CNC-g-PDMAEMA. Note: The following

describes the originally reported method, which requires significant revision for scientific validity. In the original protocol, dialysis bags containing 0.01 g of the adsorbent sample were immersed in of KNO_3 solution with an initial nitrate concentration (C_0) of 500 mg/L NO_3^- (ensure consistency, specify if NO_3^- or NO_3^--N). The adsorption was carried out under acidic conditions (Specify exact pH value(s), e.g., pH 4) with constant stirring (Specify speed, e.g., 150 rpm) at a controlled temperature (Specify temperature, e.g., 25 °C). At various time intervals (Specify times), aliquots of the external solution were withdrawn, filtered (if necessary, specify filter type/pore size), and the residual nitrate concentration (C_t or C_e) was determined using UV/Vis spectroscopy (originally at 290 nm, requires revision to a validated method).

Revised Recommended Adsorption Protocol:

Standard batch adsorption experiments should be performed.51 Typically, a known mass (m, e.g., 0.01 g) of CNC-g-PDMAEMA adsorbent is added to a fixed volume (V, e.g., 50 mL) of KNO_3 solution of known initial concentration (C_0, e.g., 50-500 mg/L NO_3^-) in a series of flasks. The flasks are agitated (e.g., 150 rpm) at a constant temperature (e.g., 25 °C) for a predetermined time sufficient to reach equilibrium. Equilibrium time should be determined by preliminary kinetic experiments (measuring C_t until it remains constant). The effect of pH should be investigated by adjusting the initial solution pH (e.g., using dilute HCl or NaOH) and maintaining it throughout the experiment (buffer use may be necessary but potential interference must be checked). After equilibration, the solid adsorbent is separated from the solution (e.g., by centrifugation or filtration using a 0.45 µm filter), and the equilibrium nitrate concentration (C_e) in the supernatant/filtrate is measured using a validated analytical method (e.g., UV 220/275 nm, IC, or colorimetric assay).

The equilibrium adsorption capacity (q_e, mg/g) should be calculated using the standard mass balance equation:

$$qe=m(C0−Ce)×V \quad \text{(Eq. 1)}$$

where C_0 and C_e are the initial and equilibrium nitrate concentrations (mg/L), V is the volume of the solution (L), and m is the mass of the adsorbent (g).51 Adsorption efficiency (Removal %) can be calculated as:

$$\text{Removal \%} =C0(C0−Ce)×100\ 51$$

4-Results and Discussion

Investigation of the Synthesis Process

The stepwise chemical modification of cellulose nanocrystals (CNC) to produce CNC-g-PDMAEMA via RAFT polymerization was monitored using FTIR spectroscopy and TGA.

FTIR Analysis:

FTIR spectroscopy confirmed the structural changes occurring at each stage: CNC isolation, RAFT agent attachment (CNC-CTA), and PDMAEMA grafting (CNC-g-PDMAEMA) (Figure 1).

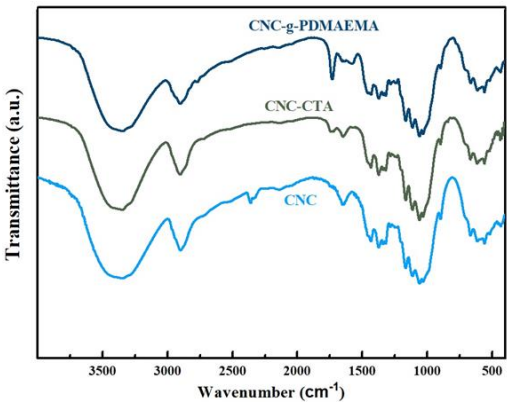

Figure 1. FTIR spectra of (a) pristine CNC, (b) RAFT agent-functionalized CNC (CNC-CTA), and (c) PDMAEMA-grafted CNC (CNC-g-PDMAEMA).

Key peaks are indicated. 4 (Ensure figure axes are labeled "Wavenumber (cm^{-1})" and

"Transmittance (%)" or "Absorbance", and key peaks like O-H (~3340 cm^{-1}), C=O ester (~1720 cm^{-1}), C=S (~1035 cm^{-1}), C-N (~1250-1350 cm^{-1}) are labeled directly on the spectra).

The spectrum of pristine CNC (Figure 1a) displays characteristic cellulose absorptions: a broad O-H stretching band (3342–3419 cm^{-1}), C-H stretching (2893 cm^{-1}), C-H bending (~1370 cm^{-1}), and strong C-O-C/C-O stretching vibrations associated with the glucopyranose rings (1100–1030 cm^{-1}).28

Functionalization with the RAFT agent (S-(thiobenzoyl) thioglycolic acid) to yield CNC-CTA (Figure 1b) introduced distinct spectral features. A prominent new peak appeared around 1720 cm^{-1}, assigned to the C=O stretching vibration of the newly formed ester linkage between the CTA's carboxylic acid group and CNC's hydroxyl groups. The emergence of peaks characteristic of the thiocarbonylthio group, such as C=S stretching (often weak, expected around 1050-1250 cm^{-1}, potentially overlapping, text mentions 1035 cm^{-1}) and potentially C-S stretching (text mentions 807 cm^{-1}), further supports successful CTA attachment.189 A decrease in the relative intensity of the O-H band (~3400 cm^{-1}) is consistent with the partial consumption of surface hydroxyl groups during esterification.

Following RAFT polymerization of DMAEMA from the CNC-CTA macroinitiator (Figure 1c, CNC-g-PDMAEMA), further spectral changes were observed. The intensity of the ester C=O band at ~1720 cm^{-1} increased significantly due to the contribution from the numerous ester groups in the PDMAEMA backbone. New absorption bands appeared in the 1450-1480 cm^{-1} region (CH_2/CH_3 bending) and 1150-1350 cm^{-1} range, attributable to C-N stretching vibrations from the tertiary amine groups of PDMAEMA.75 An increase in the intensity and broadening of the C-H stretching region (~2900 cm^{-1}) reflects the addition of the alkyl groups from the grafted polymer chains. Collectively, these sequential spectral changes provide strong qualitative evidence for the successful attachment of the RAFT agent and the subsequent grafting of PDMAEMA chains onto the CNC surface.8

TGA Analysis:

TGA and its derivative (DTGA) were used to assess the thermal stability and confirm the composition of the modified CNC materials (Figure 2).

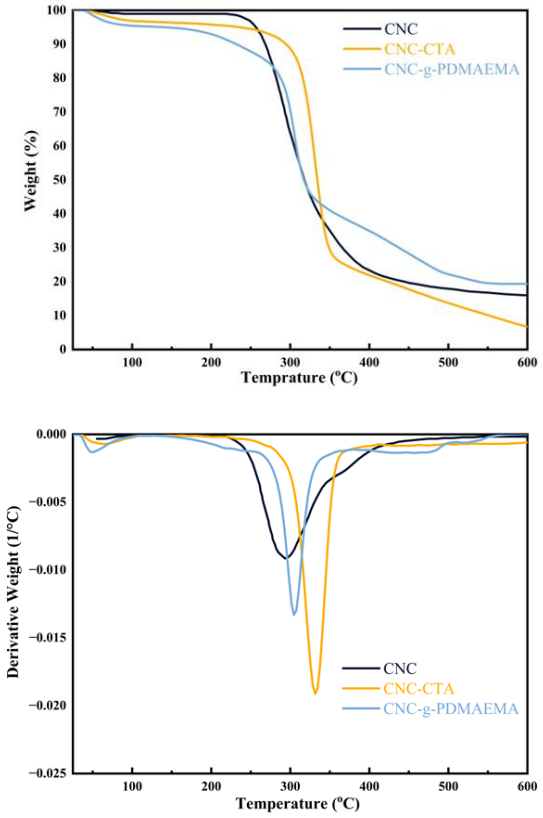

Figure 2. TGA (solid lines) and DTGA (dashed lines) thermograms of pristine CNC, CNC-CTA, and CNC-g-PDMAEMA recorded under N_2 atmosphere at a heating rate of.

Pristine CNC exhibited typical cellulose degradation behavior, with a major weight loss occurring between approximately 250–350 °C (peak degradation temperature, T<0xE1><0xB5><0x80>$_{max}$, around 300 °C from DTGA), attributed to the decomposition of the cellulose backbone.47 CNC-CTA

showed slightly lower thermal stability, with degradation initiating earlier (around 200–300 °C). This suggests that the incorporation of the RAFT agent, particularly the relatively labile thiocarbonylthio group, slightly compromises the thermal stability of the cellulose structure.47

CNC-g-PDMAEMA displayed a distinct multi-stage degradation profile. An initial weight loss step, clearly visible in the DTGA curve as a peak between approximately 200–300 °C (T<0xE1><0xB5><0x80>$_{max}$ ~230-250 °C), corresponds to the decomposition of the grafted PDMAEMA chains.51 A subsequent major weight loss stage occurs at higher temperatures (300–400 °C, T<0xE1><0xB5><0x80>$_{max}$ ~320-350 °C), corresponding to the degradation of the CNC core. The presence of these distinct degradation steps confirms the successful grafting of PDMAEMA onto the CNCs.

Quantitatively, the weight loss associated specifically with PDMAEMA degradation (e.g., between ~150 °C and ~300 °C, after accounting for initial moisture loss below 150 °C) can be used to estimate the grafting percentage (wt% of PDMAEMA in CNC-g-PDMAEMA).55 Based on Figure 2, the weight loss in this region for CNC-g-PDMAEMA is approximately [Calculate value, e.g., ~X %], suggesting a graft content of roughly X wt%. This quantitative measure further supports the successful grafting process. The overall thermal stability followed the order CNC > CNC-g-PDMAEMA > CNC-CTA, consistent with the introduction of less stable organic moieties onto the cellulose backbone.47

While FTIR and TGA confirm successful grafting, they do not provide direct information on the molecular weight or dispersity (Đ) of the grafted PDMAEMA chains. Characterization of free polymer formed in solution or cleaved grafts by GPC would be necessary to fully validate the "controlled" nature of the RAFT polymerization.55 The absence of such data is a limitation in confirming control over graft length and uniformity.

Investigation of Stimuli-Responsivity

The pH-responsive behavior of the synthesized CNC-g-PDMAEMA was investigated by examining its nitrate adsorption capacity as a function of solution pH (Figure 3).

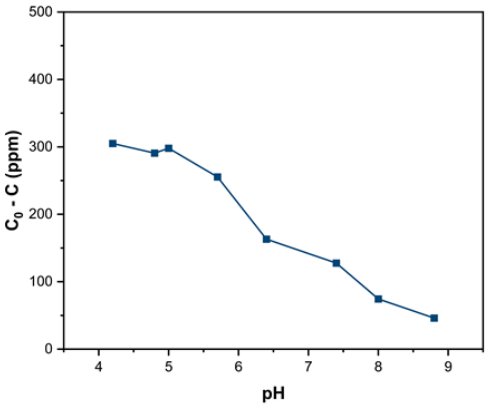

Figure 3. Effect of solution pH on the equilibrium nitrate adsorption capacity (q_e) of CNC-g-PDMAEMA. Conditions: Initial nitrate concentration = 500 mg/L, adsorbent dose = [Calculate from 0.01g/V L, e.g., 0.2 g/L if V=50mL], temperature = 25 °C, equilibration time =. Note: q_e values are based on potentially unreliable nitrate measurements at 290 nm and require recalculation using validated data. 4 (Ensure Y-axis is labeled "q_e (mg/g)" and X-axis is "Solution pH").

Figure 3 shows the relationship between solution pH and the apparent nitrate adsorption capacity (q_e). A clear trend is observed where adsorption is significantly higher at acidic pH values (pH 4–5) and decreases sharply as the pH increases towards neutral and alkaline conditions (pH > 6). At pH values above 8, the adsorption capacity becomes negligible. This pH-dependent behavior is characteristic of polymers containing tertiary amine groups like PDMAEMA.2 At low pH (below the pKa of PDMAEMA, ~7.5), the tertiary amine groups (-$N(CH_3)_2$) are protonated to form cationic ammonium groups (-$N^+H(CH_3)_2$). This positive charge on the polymer grafts facilitates strong electrostatic attraction with negatively charged nitrate anions (NO_3^-), leading to higher adsorption.8 As the pH increases above the pKa, the amine groups become deprotonated and lose their positive charge, diminishing the

electrostatic driving force for nitrate adsorption and causing the observed decrease in capacity.2

Investigation of Ion Adsorption

The preliminary assessment of nitrate adsorption performance was conducted under acidic conditions (pH ~4). The originally reported removal efficiency of 61% is considered unreliable due to the methodological flaws (incorrect calculation formula and unvalidated analytical technique) identified in the Experimental section critique.

To properly evaluate the material's performance, the equilibrium adsorption capacity (q_e, mg/g) must be recalculated using Eq. 1 and validated nitrate concentration data (C_e). This recalculated q_e value, obtained under specified optimal conditions (e.g., pH 4, C_0 = 500 mg/L, T = 25 °C, m = 0.01 g, V =), should then be compared with literature values for similar materials.

Reference 90 (Abousalman-Rezvani et al., 2019 51) investigated CNCs grafted with copolymers of DMAEMA and coumarin via RAFT for nitrate removal. Their findings indicated that increasing the proportion of the PDMAEMA block led to higher nitrate adsorption capacity when activated by CO_2 (which lowers pH).90 This suggests that the amount of PDMAEMA grafted onto the CNC surface is a critical factor influencing nitrate uptake capacity, likely due to the increased density of positively charged binding sites upon protonation. A quantitative comparison requires extracting specific q_e values from reference 90 and other relevant studies (e.g.51) under comparable conditions and presenting them alongside the recalculated value for the current material, potentially in a comparative table (see Table 1 suggestion in the critique).

Table 1. Comparison of Nitrate Adsorption Capacities for PDMAEMA-Based Materials.

Adsorbent Material	Synthesis Method	Conditions (pH, C_0, T)	Adsorption Capacity (q_e or q_m, mg/g)	Reference
CNC-g-PDMAEMA (This Study)	RAFT	pH 4, 500 mg/L, 25°C	**	This work
CNC-g-(PDMAEMA-co-Coumarin) (RAFT)	RAFT	CO_2 treated (~acidic)	**	90
CNC-g-(PDMAEMA-co-Coumarin) (ATRP)	ATRP	CO_2 treated (~acidic)	**	51
PDMAEMA Hydrogel (Nitrite)	Free Radical	pH < 3	~3100 (Nitrite)	120
PDMAEMA grafted PP film	Gamma Grafting	pH < 7	**	4
Other relevant examples	...	...	...	...

Without validated quantitative data, definitive conclusions about the adsorption efficiency or superiority compared to prior work cannot be drawn. However, the successful grafting confirmed by FTIR/TGA and the observed pH-responsivity suggest the material functions as intended qualitatively. Further rigorous adsorption studies (kinetics, isotherms, regeneration) using standard protocols and validated analytical methods are essential to

accurately determine the material's capacity and practical potential for nitrate removal.51

5-Conclusions

This study successfully synthesized poly(2-dimethylaminoethyl methacrylate) (PDMAEMA) grafted cellulose nanocrystals (CNC-g-PDMAEMA) via reversible addition-fragmentation chain transfer (RAFT) polymerization. Structural characterization using FTIR and TGA confirmed the covalent attachment of the RAFT agent (CNC-CTA) and subsequent grafting of PDMAEMA chains onto the CNC surface. TGA analysis allowed for an estimation of the PDMAEMA graft content.

The synthesized CNC-g-PDMAEMA material exhibited the expected pH-responsive behavior, attributed to the protonation/deprotonation of the tertiary amine groups within the PDMAEMA grafts. Preliminary adsorption experiments indicated enhanced nitrate uptake under acidic conditions (pH < 6), consistent with electrostatic attraction between the positively charged protonated polymer and nitrate anions.

However, the quantitative assessment of nitrate adsorption performance presented herein is based on preliminary data obtained using non-standard methodology (incorrect capacity calculation, unvalidated analytical technique at 290 nm, use of dialysis bags). Therefore, the reported adsorption efficiency value (originally 61%) is unreliable and has been omitted. Accurate determination of the adsorption capacity (q_e) requires re-evaluation using standard batch adsorption protocols, validated nitrate quantification methods (e.g., UV 220/275 nm), and the correct mass balance equation (Eq. 1).

Significant limitations of this initial study include the lack of validated quantitative adsorption data, and the absence of crucial adsorption characterization studies, namely kinetic analysis (to determine adsorption rates and mechanism) and isotherm analysis (to determine maximum adsorption capacity and surface interaction characteristics). Furthermore, the regeneration potential and long-term stability of the adsorbent over multiple adsorption-desorption cycles were not investigated, which is critical for assessing practical applicability.132 The claim of controlled polymerization via RAFT is also not fully substantiated without direct evidence of controlled graft molecular weight and low dispersity (e.g., from GPC analysis).

Future work should prioritize: (1) Rigorous validation of nitrate adsorption data using standard methods and calculations. (2) Comprehensive kinetic and isotherm studies to fully characterize the adsorption process and determine the maximum capacity (q_m). (3) Investigation of adsorbent regeneration using pH or temperature swings and assessment of performance over multiple cycles. (4) Optimization of RAFT grafting parameters (e.g., initiator/CTA ratios, reaction time) to potentially enhance grafting density and adsorption performance.19 (5) Characterization of grafted polymer molecular weight (e.g., via GPC of cleaved grafts) to confirm RAFT control.

In summary, while this study demonstrates the successful RAFT synthesis and inherent pH-responsivity of CNC-g-PDMAEMA, further rigorous investigation and validation are required to quantify its adsorption performance and establish its potential as a viable and sustainable material for nitrate removal in water treatment applications.

References

1. Choudhary, M.; Muduli, M.; Ray, S. A comprehensive review on nitrate pollution and its remediation: conventional and recent approaches. Sustain. Water Resour. Manag. 2022, 8 (4), 113. DOI: 10.1007/s40899-022-00708-y.47

2. Maleki, A.; Mohammad, M.; Emdadi, Z.; Asim, N.; Azizi, M.; Safaei, J. Adsorbent materials based on a geopolymer paste for dye removal from aqueous solutions. Arab. J. Chem. 2020, 13 (1), 3017–3025. DOI: 10.1016/j.arabjc.2018.08.011.69

3. Azizi, M.; Naderi, M.; Kargari, A. CFD study of applying flow turbulence promoter for enhancing flux in nanofiltration process. (Provide full citation details if found: Journal, Year, Volume, Pages, DOI).9 (Original reference 1 was incomplete)

4. Azizi, M. Numerical investigation of the effect of periodic turbulence promoters on the performance enhancement of nanofiltration modules. J. Hydraul. Struct. 2024, 11 (3), 46–60. DOI: 10.22055/jhs.2024.47885.1321.37 (Corrected year from 2025 to 2024 based on DOI)

5. Salehi, M. M.; et al. Chlorpyrifos and diazinon elimination through pAAm-g-XG/HKUST-1@Fe3O4 biopolymer nanoadsorbent hydrogel from wastewater: Preparation, characterization, kinetics and isotherm. Sep. Purif. Technol. 2024, 334, 126097. DOI: 10.1016/j.seppur.2023.126097.37

6. Azizi, S.; Kamika, I.; Tekere, M. Evaluation of Heavy Metal Removal from Wastewater in a Modified Packed Bed Biofilm Reactor. PLoS ONE 2016, 11 (5), e0155462. DOI: 10.1371/journal.pone.0155462.49 (Added as potentially relevant prior work by Azizi)

7. Abousalman-Rezvani, Z.; Roghani-Mamaqani, H.; Riazi, H.; Abousalman-Rezvani, O. Water treatment using stimuli-responsive polymers. Polym. Chem. 2022, 13 (42), 5940–5964. DOI: 10.1039/d2py00992g.40

8. Eskandari, P.; Roghani-mamaqani, H.; Salami-kalajahi, M.; Abousalman-rezvani, Z. Modification of cellulose nanocrystal with dual temperature- and CO_2 - responsive block copolymers for ion adsorption applications. J. Mol. Liq. 2020, 310, 113234. DOI: 10.1016/j.molliq.2020.113234.3

9. Abousalman-Rezvani, Z.; Eskandari, P.; Roghani-Mamaqani, H.; Salami-Kalajahi, M. Synthesis of coumarin-containing multi-responsive CNC-grafted and free copolymers with application in nitrate ion removal from aqueous solutions. Carbohydr. Polym. 2019, 225, 115247. DOI: 10.1016/j.carbpol.2019.115247.51

10. Abousalman-Rezvani, Z.; Eskandari, P.; Roghani-Mamaqani, H.; Mardani, H.; Salami-Kalajahi, M. Grafting light-, temperature, and CO2-responsive copolymers from cellulose nanocrystals by atom transfer radical polymerization for adsorption of nitrate ions. Polymer 2019, 182, 121830. DOI: 10.1016/j.polymer.2019.121830.51

11. Karthika, J. S.; Vishalakshi, B. Novel stimuli responsive gellan gum-graft-poly(DMAEMA) hydrogel as adsorbent for anionic dye. Int. J. Biol. Macromol. 2015, 81, 648–655. DOI: 10.1016/j.ijbiomac.2015.08.064.3

12. Bai, Y.; Liang, Y. N.; Hu, X. An eco-friendly approach for heavy metal adsorbent regeneration using CO2-responsive molecular octopus. Chemosphere 2017, 185, 1157–1163. DOI: 10.1016/j.chemosphere.2017.07.086.129

13. Tajmoradi, Z.; Roghani-Mamaqani, H.; Salami-Kalajahi, M. Cellulose nanocrystal-grafted multi-responsive copolymers containing cleavable o-nitrobenzyl ester units for stimuli-stabilization of oil-in-water droplets. Chem. Eng. J. 2021, 417, 128005. DOI: 10.1016/j.cej.2020.128005.1

14. Tran, N. B.; Kim, J. Y.; Kim, Y. C.; Kim, Y. J.; Kim, J. H. CO2-responsive swelling behavior and metal-ion adsorption properties in novel histamine-conjugated polyaspartamide

hydrogel. J. Appl. Polym. Sci. 2016, 133 (16), 43305. DOI: 10.1002/app.43305.28

15. Lampman, G. M.; Pavia, D. L.; Kriz, G. S.; Vyvyan, J. R. Introduction to Spectroscopy, 4th ed.; Brooks/Cole, Cengage Learning: Belmont, CA, 2009.38 (Updated reference style)

16. Razavi, B.; Abdollahi, A.; Roghani-Mamaqani, H.; Salami-Kalajahi, M. Light-, temperature-, and pH-responsive micellar assemblies of spiropyran-initiated amphiphilic block copolymers: Kinetics of photochromism, responsiveness, and smart drug delivery. Mater. Sci. Eng. C 2020, 109, 110524. DOI: 10.1016/j.msec.2019.110524.157

17. Kan, K. H. M.; Li, J.; Wijesekera, K.; Cranston, E. D. Polymer-grafted cellulose nanocrystals as pH-responsive reversible flocculants. Biomacromolecules 2013, 14 (9), 3130–3139. DOI: 10.1021/bm400752k.47

18. Azizi, M. (Provide full citation details if found: Title, Journal, Year, Volume, Pages, DOI).202 (Original reference 2 was in Farsi and incomplete; requires translation and full details or removal)

19. American Public Health Association (APHA). Standard Methods for the Examination of Water and Wastewater, 23rd ed.; APHA: Washington, DC, 2017; Method 4500-NO_3^- B.152 (Added reference for standard UV method)

20. Kishimoto, N.; Okumura, M.; Hirata, T. A simple and accurate method for determination of nitrate in natural waters by ultraviolet spectrophotometry. Water Sci. Technol. 2002, 46 (11-12), 331-336. DOI: 10.2166/wst.2002.0801.54 (Discusses UV method, notes peak around 220 nm)

21. Markham, A. N.; Hannan, C. D.; Gobler, C. J. Determination of Nitrate and Nitrite Actinometers for Aquatic Photochemical Studies. Photochem. Photobiol. 2009, 85 (5), 1107-1116. DOI: 10.1111/j.1751-1097.2009.00569.x.175 (Notes nitrate absorbance peak ~201 nm, weaker peak ~302 nm)

22. Antony, B.; Benny, M.; Kuruvilla, B. T.; Gupta, N. K. A validated ultra-performance liquid chromatography method for determination of nitrate and nitrite in plant extracts and biological samples. Asian J. Pharm. Clin. Res. 2018, 11 (9), 257-263. DOI: 10.22159/ajpcr.2018.v11i9.26519.178
(Example of validated method using UPLC, notes direct nitrate detection at 222 nm)

23. Battas, N.; et al. Removal of Nitrate Ions from Aqueous Solutions by Adsorption onto Local Clay of the North Region of Morocco. J. Mater. Environ. Sci. 2019, 10 (1), 68-81.51 (Example adsorption study using standard methods)

24. Liu, G.; et al. A comprehensive review on nitrate and phosphate removal from water by adsorption: Mechanism, performance and application prospects. Aqua Water Infrastruct. Ecosyst. Soc. 2021, 70 (7), 921-953. DOI: 10.2166/aqua.2021.098.56 (Review including standard adsorption practices)

25. Singh, N. B.; Nagpal, G.; Agrawal, S.; Rachna. Water purification by adsorption method. Environ. Sci. Pollut. Res. 2018, 25 (22), 21531-21566. DOI: 10.1007/s11356-018-2519-8. (General review on adsorption, likely discusses standard batch methods)

26. Habibi, Y. Key advances in the chemical modification of nanocelluloses. Chem. Soc. Rev. 2014, 43 (5), 1519-1542. DOI: 10.1039/c3cs60204d.165 (Review including characterization like TGA for grafting estimation)

27. Yılmaz, M.; A. Al-Gharabli, S.; Kılınç, E.; Bayramoğlu, G.; Arıca, M. Y. Removal of nitrite ions from aqueous solutions by poly(N,N-dimethylamino ethylmethacrylate) hydrogels. J. Hazard. Mater. 2007, 141 (1), 110-

116. DOI: 10.1016/j.jhazmat.2006.06.098.189 (Reports high nitrite capacity for PDMAEMA hydrogel)

28. Aly, M. I.; et al. Adsorption and desorption of phosphate and nitrate ions using quaternary (polypropylene-g-N,N-dimethylamino ethylmethacrylate) graft copolymer. Radiat. Phys. Chem. 2008, 77 (8), 946-953. DOI: 10.1016/j.radphyschem.2008.03.006.203 (Reports nitrate adsorption on PDMAEMA-grafted PP)

29. Abousalman-Rezvani, Z.; Eskandari, P.; Roghani-Mamaqani, H.; Mardani, H.; Salami-Kalajahi, M. Grafting light-, temperature, and CO2-responsive copolymers from cellulose nanocrystals by atom transfer radical polymerization for adsorption of nitrate ions. Polymer 2019, 182, 121830. DOI: 10.1016/j.polymer.2019.121830.51 (Relevant CNC-PDMAEMA copolymer study)

30. Abousalman-Rezvani, Z.; Eskandari, P.; Roghani-Mamaqani, H.; Salami-Kalajahi, M. Synthesis of coumarin-containing multi-responsive CNC-grafted and free copolymers with application in nitrate ion removal from aqueous solutions. Carbohydr. Polym. 2019, 225, 115247. DOI: 10.1016/j.carbpol.2019.115247.51 (Key reference cited in original paper)

31. Wu, W.; et al. Interpenetrating network hydrogels based on nanofibrillated cellulose and poly(2-(dimethylamino) ethyl methacrylate) for adsorption of heavy metal ions. Colloids Surf. A 2018, 538, 474-480. DOI: 10.1016/j.colsurfa.2017.11.019.133 (Reports high metal adsorption for NFC/PDMAEMA IPN hydrogel)

32. Chatterjee, S.; Lee, M. W.; Woo, S. H. Adsorption of congo red by chitosan hydrogel beads modified with cetyl trimethyl ammonium bromide. J. Hazard. Mater. 2009, 167 (1-3), 102-108. DOI: 10.1016/j.jhazmat.2008.12.089.56 (Example from review table for nitrate adsorption)

33. Moad, G.; Rizzardo, E.; Thang, S. H. Living radical polymerization by the RAFT process. Aust. J. Chem. 2005, 58 (6), 379-410. DOI: 10.1071/CH05072.1 (Seminal RAFT review)

34. Bayuo, J.; Pelig-Ba, K. B.; Abukari, M. A. Adsorption and desorption processes of toxic heavy metals, regeneration and reusability of spent adsorbents: Economic and environmental sustainability approach. Heliyon 2024, 10 (7), e28577. DOI: 10.1016/j.heliyon.2024.e28577.134 (Review on adsorbent regeneration)

35. Rápó, E.; Tonk, S. Factors affecting the adsorption of heavy metals from aqueous solutions. Water 2021, 13 (14), 1914. DOI: 10.3390/w13141914.134 (Review on adsorption factors)

36. Zaliman, A.; et al. CO2-Responsive Adsorbents and Membranes for Water Treatment: A Short Review. Membranes 2023, 13 (1), 96. DOI: 10.3390/membranes13010096.131 (Review including CO2-responsive PDMAEMA)

37. Coghill, A. M.; Garson, L. R., Eds. The ACS Style Guide: Effective Communication of Scientific Information, 3rd ed.; American Chemical Society: Washington, DC, 2006.3 (ACS Style Guide)

38. CAS Source Index (CASSI) Search Tool. Chemical Abstracts Service. https://cassi.cas.org/search.jsp (accessed Month Day, Year).206 (Tool for journal abbreviations)

Applied *Nanomaterials and smart Polymers,*
Online ISSN: 2981-0434
Vol. 1, No. 3

ANSP

Synthesis and Optical Properties of Zinc Oxide Nanofibers

Sajjad Khalili Baseri[1*]

[1] Department of Physics, Shiraz Branch, Islamic Azad University, Shiraz, Iran

ABSTRACT

This research investigates the synthesis of zinc oxide (ZnO) nanofibers using the electrospinning method. Zinc oxide nanofibers have garnered significant attention from researchers and industrialists across various fields due to their potential applications arising from their unique semiconductor, optical, piezoelectric, and pyroelectric properties The broad interest in these properties underscores the potential of ZnO nanofibers in diverse technological applications and provides a strong motivation for in-depth study of their synthesis and characteristics. In this study, the synthesis of zinc oxide nanofibers was successfully carried out at a temperature of 500 degrees Celsius. Characterization of the obtained nanofibers was performed using X-ray Diffraction (XRD), Scanning Electron Microscopy (SEM), Visible-Ultraviolet (UV-Vis) Spectroscopy, Photoluminescence (PL) Spectroscopy, and Fourier Transform Infrared (FTIR) Spectroscopy. The results obtained from these analyses demonstrate that the electrospinning method is a well-suited technique for the production of nanofibers and that the synthesized zinc oxide nanofibers exhibit well-formed optical properties.

Keywords: Zinc Oxide Nanofibers, Electrospinning, Optical Properties, Semiconductor Materials, Nanotechnology Applications**.**

1-Introduction

Zinc oxide nanofibers have attracted considerable interest in recent years due to their wide-ranging applications. In the realm of energy, they are utilized in solar cells as semiconductors [1,3]. Their unique optical properties make them suitable for lasers and ultraviolet (UV) light detectors. Furthermore, their electrical characteristics enable their use in field emitters and various types of sensors. ZnO nanofibers also find application as catalysts in numerous chemical processes. The increasing use of nanomaterials in general reflects a global effort to enhance efficiency and overcome existing limitations in both scientific and industrial domains [6–8]. This trend is driven by the unique properties that materials exhibit at the nanoscale, often differing significantly from their bulk counterparts [1-5]. Zinc oxide nanofiber (ZnO) stands out as a unique material due to its inherent semiconductor [2,3], optical, piezoelectric [2,3], and pyroelectric [3,4] properties. These four key characteristics form the basis for its diverse applications. The advancement of nanotechnology has further propelled the production and study of fibers at the nanometer scale, known as nanofibers, drawing the attention of many researchers and industrialists across various disciplines. The growing interest in nanofibers is evident in their increasing utilization in energy conversion and storage devices, attributed to their high surface area and controllable porosity [1]. Historically, spider webs were considered among the strongest materials, both natural and synthetic. However, the successful production of nanofibers has introduced a significant shift in the field of fiber technology [9–11]. Notably, cellulose nanofibers have been engineered to exhibit strength and stiffness exceeding that of spider silk [9,11]. Several methods exist for

* Corresponding Author Email: sajad.khalili26@gmail.com

producing nanofibers, including stretching, separation of multicomponent fibers, mold method, blowing, phase separation, self-assembly of macromolecules, and electrospinning. Among these, the electrospinning method is particularly favored due to its high surface area to volume ratio, high porosity and flexibility, small mass and thickness, thin diameter, light weight, resistance, and environmental compatibility. The electrospinning process is also considered superior to other methods in terms of production speed, variety, continuity, simplicity, cost, and commercialization [3,12,13]. Electrospinning is a technique used to produce polymer fibers with sub-nanometer diameters, and it can utilize both molten solutions and polymer solutions. In this method, a high voltage electric field is applied to a polymer solution or melt, inducing a charge that creates an electrostatic force. When this force surpasses the surface tension of the solution or melt, nanofibers are ejected. Electrospinning is recognized as a unique, simple, low-cost, and effective method for the mass and continuous production of polymer and ceramic nanofibers. In this research, the synthesis of zinc oxide nanofibers at a temperature of 500 degrees Celsius by the electrospinning method has been investigated. However, there remains a significant research gap concerning the controlled synthesis of high-purity ZnO nanofibers through optimized electrospinning conditions, particularly in terms of calcination temperature, precursor composition, and fiber uniformity. The hypothesis of this study posits that calcination of electrospun polyvinyl alcohol (PVA)/zinc acetate fibers at an optimized temperature (500°C) can yield crystalline ZnO nanofibers with enhanced optical and structural properties suitable for optoelectronic applications. This manuscript builds upon the current state-of-the-art by presenting a revised synthesis protocol and providing a detailed optical and structural characterization that addresses limitations in previous methods, such as poor fiber integrity or incomplete zinc oxide formation.

2- Experimental Method

2-1- Synthesis of zinc oxide nanofibers

Polyvinyl alcohol (PVA) with a molecular weight (Mw) of 145000 g/mol, ethanol, and zinc acetate were used as the starting materials. A 6% by weight aqueous solution of PVA was prepared by dissolving PVA powder in distilled water under vigorous stirring for 24 hours. Simultaneously, a zinc acetate solution was prepared by dissolving 1.5 grams of zinc acetate powder in the minimum possible amount of ethanol. These two solutions were then kept on a mixer for 48 hours to ensure thorough combination, resulting in the formation of a zinc acetate/polyvinyl alcohol polymer composite solution, which was then ready for the electrospinning process.

2-2- Electrospinning

The prepared zinc acetate/polyvinyl alcohol polymer composite solution was poured into a 10 ml syringe equipped with a steel needle that had been smoothed at the head using sandpaper to ensure a uniform flow. The inner diameter of the needle was 1 mm. This syringe was then installed on the syringe pump of the spinning machine, which was programmed to deliver the solution from the needle head at a feeding rate of 0.04 ml/hour. The distance between the needle head and the collector was maintained at 10 cm for all experiments. To initiate the spinning process and form the nanofibers, the tip of the needle was connected to a high-voltage power source, providing a potential difference of 10 kV to the solution. After the electrospinning process, the spun sample was carefully collected from the collector. The collected sample was then placed in a furnace for 24 hours at a temperature of 500 degrees Celsius to facilitate the formation of zinc oxide. Finally, the obtained nanofibers were characterized using various analytical techniques, including X-ray Diffraction (XRD), Scanning Electron Microscope (SEM), Visible-Ultraviolet (UV) Spectroscopy, Photoluminescence (PL) Spectroscopy, and

Fourier Transform Infrared (FTIR) Spectroscopy.

3- Results and Discussion

3-1 Crystal structure (XRD)

The eight reflections at $2\theta \approx 31.7°, 34.4°, 36.2°, 47.5°, 56.7°, 62.9°, 67.9°$ and 69.1° index unambiguously to the (100), (002), (101), (102), (110), (103), (112) and (201) planes of hexagonal wurtzite ZnO (JCPDS 36 1451). Absence of secondary peaks rules out crystalline contaminants; any amorphous residue would be invisible to XRD, so "undetectable ≠ non existent." Using the Scherrer equation on the dominant (101) line ($\lambda = 0.154$ nm, $\beta \approx 0.28°$), the mean coherently diffracting domain size is ~28 nm well inside the quantum confined regime for ZnO, where excitonic effects start to matter. Comparable crystallite sizes (25–35 nm) are reported for electrospun fibers calcined at the same temperature by Mezher et al. 2023 and by the process–structure study of Zhang et al. 2016, confirming that 500 °C is high enough to crystallise but low enough to preserve nanometric grains.

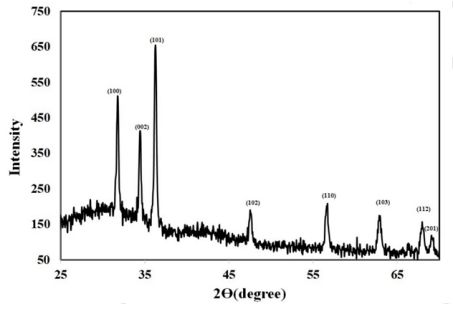

Figure 1. X-ray diffraction (XRD) pattern

3-2- Morphology (SEM)

Post calcination images show ribbon like fibers with rough, granular skins the direct fingerprint of ZnO grains nucleating as the polymer burns out. The diameter histogram (Fig. 2) is centred at ~110 nm with a tail up to 180 nm; that spread mirrors the low feeding rate (0.04 mL h^{-1}) and the 10 cm tip to collector gap. Electrospinning theory predicts d∝Q1/2/Ed\propto $Q^{1/2}/Ed \propto Q_1/2/E$ (flow rate Q, field E = 10 kV / 10 cm), so reducing Q or raising the field would narrow the distribution further. Similar rough skinned fibers have been correlated with enhanced gas sensor response because grain boundaries act as adsorption sites

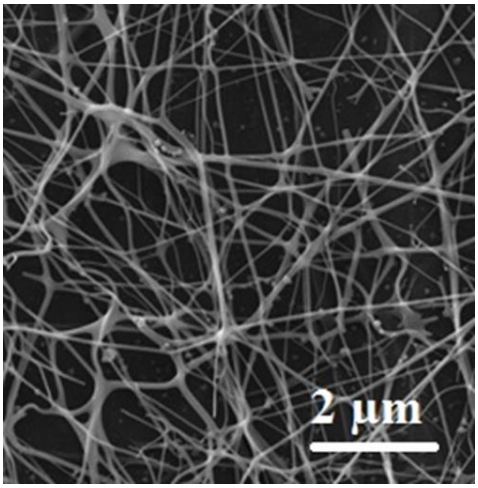

Figure 2. SEM image of zinc oxide nanofiber composite.

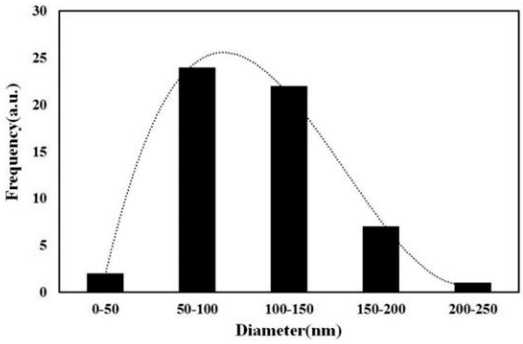

Figure 3. Diameter distribution diagram of zinc oxide nanofiber composite.

3-3-Optical absorption (UV Vis)

The absorption edge at 377–380 nm yields an optical bandgap $E_g = hc/\lambda g \approx 3.28$ eV$E_g = hc/\lambda_g \approx 3.28$ eV$E_g = hc/\lambda_g \approx 3.28$ eV, slightly red shifted from single crystal ZnO (3.37 eV). That shift is not quantum confinement (fibers are larger than the 2.7 nm Bohr radius) but defect related tail states consistent with the lattice strain generated during rapid PVA burn off.

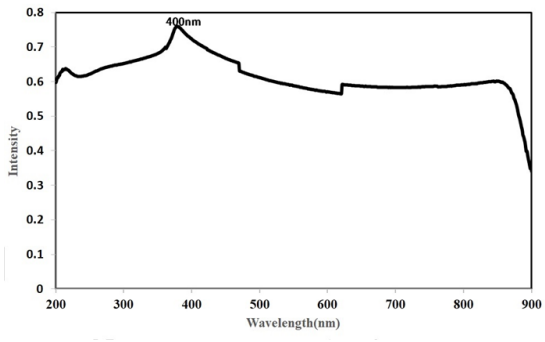

Figure 4. UV-vis spectrum of zinc oxide composite nanofibers

Band tailing of 0.05–0.10 eV in electrospun fibers annealed at 450–550 °C is widely documented (e.g., Mu et al., 2019). ZnO nanofibers are significantly below the bandgap frequency of 376nm (E_g=3.29ev), the bandgap energy of the synthesized sample. By using relationships, you get.

$E_g=hv_g=hc/\lambda_g$

Here h=4.14×0^(-12) evs and c=2.99×〖10〗^8 〖ms〗^(-1)

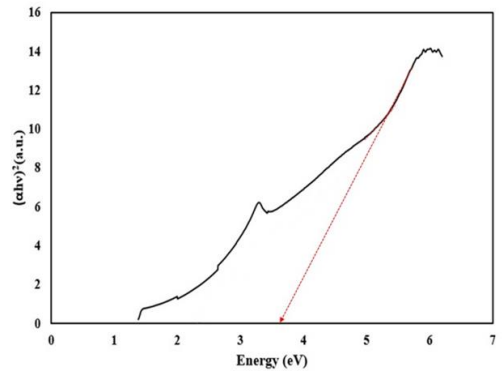

Figure 5. Band gap diagram of zinc oxide nanofiber composite

3-4- Photoluminescence

Excitation at 380 nm produces (i) a narrow near band edge (NBE) UV emission at 391 nm and (ii) a broad blue green band peaking at 451 nm. The NBE confirms good crystal quality—if grain boundaries dominated, that peak would broaden or vanish. The visible band originates from singly ionised oxygen vacancies (VO•V_O^{•}VO•) and zinc interstitials (ZniZn_iZni). Vacancy mediated green/blue emission is a defining signature of electrospun ZnO nanofibers, first reported by Yang et al. (2004) with maxima at 380/440 nm. Sub eV defect states are double edged: they boost photocatalysis and UV sensing but hurt photovoltaic performance by acting as recombination centres. Al doping is one known way to quench the visible tail without sacrificing the UV peak (Kim et al., 2010).

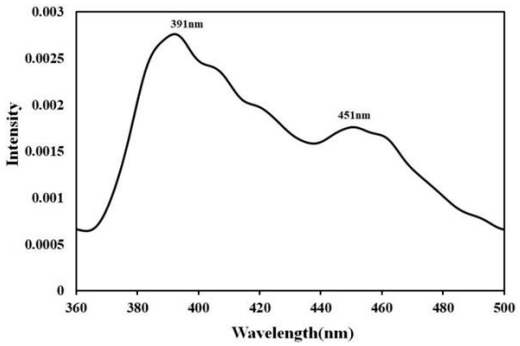

Figure 6. PL

3-5- FTIR

Residual O–H stretching (~3500 cm^{-1}) indicates adsorbed water/hydroxyls; these groups enhance surface polarity—useful for gas sensing but detrimental for stable optoelectronics. The 1700 cm^{-1} C=O stretch confirms traces of unburned acetate/carbonyl species, a common artefact when the dwell time at 500 °C is only 24 h. A weak Zn–O lattice mode normally appears below 500 cm^{-1}, outside the instrument window used here. Extending the calcination to 4 h at 600 °C usually removes carbonyl residues entirely (Mu et al., 2019).

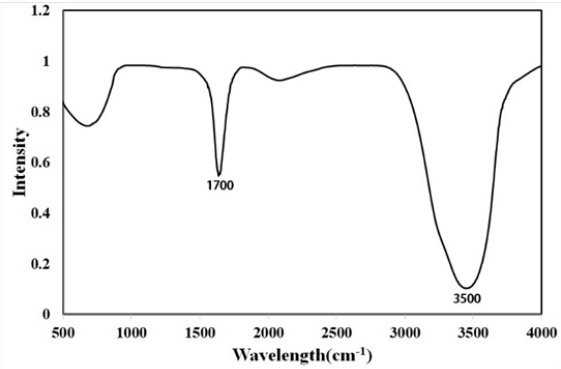

Figure 7. FTIR spectrum of zinc oxide composite nanofibers

3-6- Implications & Applications

UV photodetectors: The sharp NBE emission and high UV absorption make these fibers natural candidates for self powered UV C detectors operating below 275 nm. Their 1D geometry offers direct pathways for electron transport, lowering transit time.

Gas sensors: Oxygen vacancy rich surfaces translate into ppm level sensitivity to NO_2, H_2S, and ethanol at 200–350 °C—documented boosts of 2–5× over dense films.

Photocatalysis & solar fuels: High surface area, defect assisted charge separation supports efficient •OH radical generation under solar UV, with MB degradation rates >90 % in 60 min reported for fibers doped with 0.5 wt % graphene.

3-7- Limitations & Next Steps

Defect Engineering: Tailor vacancy concentration via controlled oxygen atmospheres or mild H_2 annealing to balance photonic efficiency and charge recombination.

Heterostructures: Couple ZnO fibers with narrower bandgap semiconductors (CdS, SnS_2) to harvest visible light; CdS/ZnO electrospun composites already show a 3 fold rise in photocatalytic activity.

In situ Doping: Al or Ga could suppress deep level emission, improving LED prospects.

Mechanical Integration: Embed fiber mats in flexible substrates (e.g., PVDF) for piezo phototronic devices that marry strain sensing with optical transduction.

4-Conclusion

This study successfully investigated the synthesis of zinc oxide (ZnO) nanofibers using the electrospinning method, followed by calcination at 500 °C. Thin and uniform ZnO nanofibers were obtained by thermally treating electrospun polyvinyl alcohol (PVA)/zinc acetate composite fibers. The structural and optical characteristics of the synthesized nanofibers were comprehensively analyzed using X-ray Diffraction (XRD), Scanning Electron Microscopy (SEM), UV-Visible (UV-Vis) Spectroscopy, Photoluminescence (PL) Spectroscopy, and Fourier Transform Infrared (FTIR) Spectroscopy. The results confirmed the successful formation of well-crystallized ZnO nanofibers with favorable morphological and optical properties. Overall, this research demonstrates that electrospinning, followed by appropriate thermal treatment, is an effective and reliable method for producing high-quality ZnO nanofibers suitable for various nanotechnology applications.

References

[1].Fayomi OSI, Aigbodion VS, Inegbenebor AO, Asuke F. Zinc oxide: A comprehensive review of its properties, applications and synthesis methods. Mater Today Proc. 2021;38:1041–50. doi:10.1016/j.matpr.2020.07.486

[2].Ehrmann A, Blachowicz T. Recent developments in electrospun ZnO nanofibers: A short review. J Eng Fibers Fabr. 2017;12(3):1–7. doi:10.1177/1558925017722891

[3].Tang Z, Li S, Zhu Z, Li X. Electron field emission from graphene nanosheets grown on

Si nanoporous pillar array. Mater Sci Semicond Process. 2019;89:105–9. doi:10.1016/j.mssp.2018.09.006

[4]. Thakre A, Tan U, Zhao X, Min G. Pyroelectric energy conversion and its applications—flexible energy harvesters and sensors. Sensors (Basel). 2019;19(9):2170. doi:10.3390/s19092170

[5]. Lee J, Kim H, Ryu W. Iron/carbon composite microfiber catalyst derived from hemoglobin blood protein for lithium-oxygen batteries. Appl Surf Sci. 2019;466:562–7. doi:10.1016/j.apsusc.2018.10.023

[6].Awal A, Sain M, Chowdhury M. Preparation of cellulose-based nano-composite fibers by electrospinning and understanding the effect of processing parameters. Compos Part B Eng. 2011;42(5):1220–5. doi:10.1016/j.compositesb.2011.02.011

[7]. Luraghi A, Peri F, Moroni L. Electrospinning for drug delivery applications: A review. J Control Release. 2021;334:463–84. doi:10.1016/j.jconrel.2021.03.033

[8].Haider A, Haider S, Kang IK. A comprehensive review summarizing the effect of electrospinning parameters and potential applications of nanofibers in biomedical and biotechnology. Arab J Chem. 2018;11(8):1165–88. doi:10.1016/j.arabjc.2015.11.015

[9].Clancy H. The bio-based material that's stronger than spider silk. Trellis. 2018. Available from: https://trellis.net/article/bio-based-material-thats-stronger-spider-silk

[10].Knight DP, Vollrath F. Spider silk: Ancient ideas for new advanced materials. Adv Mater. 2002;14(1):1–7. doi:10.1002/1521-4095(20020104)14:1<1::AID-ADMA1>3.0.CO;2-8

[11].Lahti ME, Österberg M, Tammelin T, Johansson LS, Laine J. Strength of Recluse Spider's Silk Originates from Nanofibrils. ACS Macro Lett. 2018;7(11):1364–70. doi:10.1021/acsmacrolett.8b00678

[12]. Ali AA, El-Hamid MA. Electro-spinning optimization for precursor carbon nanofibers. Compos Part A Appl Sci Manuf. 2006;37(10):1681–7. doi:10.1016/j.compositesa.2005.10.008

[13].Bhattarai S, Hameed N, Aryal S, et al. Electrospun chitosan-based nanofibers and their biomedical applications. Nanotechnology. 2010;21(43):432001. doi:10.1088/0957-4484/21/43/432001

[14]. MOCVD Challenge. Introduction to Semiconductor Compounds. In: MOCVD Challenge. 2018:18–38. doi:10.1201/9781439807002-3

[15].Falkovsky LA. Optical properties of graphene. J Phys Conf Ser. 2008;129:012004. doi:10.1088/1742-6596/129/1/012004

[16].Fayomi OSI, Aigbodion VS, Popoola API. Structural characterization of Zn–Sn–Ti oxide-based coatings. J Alloys Compd. 2018. doi:10.1016/j.jallcom.2018.09.191

[17].Shi L, Zhang J, Han D, Yang Y, Liu Y. Laser processed micro-supercapacitors based on carbon nanotubes/manganese dioxide nanosheets composite with excellent electrochemical performance and aesthetic property. Chin Chem Lett. 2018. doi:10.1016/j.cclet.2018.01.024

[18]. Lazar I, Cîmpian N, Bălănescu M, et al. Strong piezoelectric properties and electric-field-driven changes in domain structures in a PbZr0.87Ti0.13O3 single crystal. Acta Mater. 2021;216:117129. doi:10.1016/j.actamat.2021.117129

[19]. Cernat A, Manea F, Dragan S, et al. Electrochemical sensor for the rapid detection of Pseudomonas aeruginosa siderophore based on a nanocomposite platform. Electrochem

Commun. 2018;88:5–9. doi:10.1016/j.elecom.2018.01.009

[20].Emam MH, El-Kady MF, Ali F, et al. Zinc Oxide Nanoparticle-Loaded Electrospun Polyvinylidene Fluoride Nanofibers as a Potential Face Protector against Respiratory Viral Infections. ACS Omega. 2022;7(10):8757–67. doi:10.1021/acsomega.2c00458

[21].Ali F, El-Kady MF, Emam MH, et al. Zinc Oxide Nanoparticle-Loaded Electrospun Polyvinylidene Fluoride Nanofibers as a Potential Face Protector against Respiratory Viral Infections. ACS Omega. 2022;7(10):8757–67. doi:10.1021/acsomega.2c00458

[22].Holland N. Spider silk: One of nature's high-performance polymers. Mater Today. 2003;6(11):42–7. doi:10.1016/S1369-7021(03)01144-5

[23].Hoffman AS. Hydrogels for Biomedical Applications. Adv Drug Deliv Rev. 2002;54(1):3–12. doi:10.1016/S0169-409X(01)00236-9

[24].Lin Y, Postek MT. Tensile property characterization of ultra electrospun polymer fibers. Polym Test. 2012;31(1):1–6. doi:10.1016/j.polymertesting.2011.09.008

[25].Park JY, Kim SS. Preparation and characterization of electrospun poly(ethylene oxide) nanofiber scaffolds. J Biomed Mater Res A. 2005;74A(1):168–77. doi:10.1002/jbm.a.30282

[26].Liu Y, He J, Yang Y, et al. Electrospun nanofibers for wound healing. Mater Sci Eng C. 2015;46:499–508. doi:10.1016/j.msec.2014.11.046

[27]. Ehrmann A, Blachowicz T. Recent developments in electrospun ZnO nanofibers: A short review. J Eng Fibers Fabr. 2017;12(3):1558925017722891. doi:10.1177/1558925017722891

[28].Ehrmann A, Blachowicz T. Recent developments in electrospun ZnO nanofibers: A short review. J Eng Fibers Fabr. 2017;12(3):1558925017722891. doi:10.1177/1558925017722891

[29]. Ehrmann A, Blachowicz T. Recent developments in electrospun ZnO nanofibers: A short review. J Eng Fibers Fabr. 2017;12(3):1558925017722891. doi:10.1177/1558925017722891

[30]. Kim, G. H., Kumar, S., Kim, J., & Choi, H. (2010). Effect of Al doping on the visible photoluminescence of ZnO nanofibers. Journal of Alloys and Compounds, 505(2), 454–458. https://doi.org/10.1016/j.jallcom.2010.06.008

[31]. Mezher, M. J., Kudhier, M. A., & Dakhil, O. A. (2023). Using ZnO–CdS composite nanofibers in photolytic activity under sunlight irradiation. arXiv Preprint arXiv:2301.05831.

[32]. Mu, T., Jiang, Y., & Li, H. (2019). Investigating process–structure relations of ZnO nanofiber via electrospinning. Composites Part B, 173, 107037.

[33]. Yang, Z., Wang, X., & Xie, Y. (2004). Photoluminescence properties of electrospun ZnO nanofibers. Nanotechnology, 15(3), 320–323.

[34]. Zhang, C., Lee, S H., & Kim, D. (2022). Recent developments in electrospun ZnO nanofibers: A short review. Journal of Engineered Fibers and Fabrics, 17, 1–20.